Astron. Astrophys. 283, 525–560 (1994)

ASTRONOMY
AND
ASTROPHYSICS

Radiation-driven winds of hot luminous stars

XII. A first step towards detailed UV-line diagnostics of O-stars

A.W.A. Pauldrach[1], **R.P. Kudritzki**[1,2], **J. Puls**[1], **K. Butler**[1], **and J. Hunsinger**[1]

[1] Institut für Astronomie und Astrophysik der Universität München, Scheinerstr. 1, D-81679 München, Germany
[2] Max-Planck-Institut für Astrophysik, Karl-Schwarzschildstr. 1, D-85748 Garching bei München, Germany

Received 26 April 1993 / Accepted 3 July 1993

Abstract. Improved radiation driven wind models are constructed to calculate detailed synthetic UV spectra of hot luminous stars. The model improvements comprise: a very detailed multilevel NLTE treatment of 29 of the most important ionization stages, in particular C, N, O and Fe using accurate atomic data; the approximate inclusion of EUV radiation by shock heated matter in the ionization rates and a simple simulation of photospheric line blocking.

Due to the improved NLTE opacities the calculated rates of mass-loss are increased by nearly a factor of two relative to previous models.

The direct ionization by EUV shock radiation has important effects on the lines of the highest ionization stages, whereas line blocking is needed to reproduce the lowest stages of ionization that are observed.

A detailed comparison between observed and calculated synthetic spectra of two O-stars, ζ Puppis in the Galaxy and Melnick 42 in the LMC, has been carried out to develop diagnostic tools for the determination of stellar parameters, abundances and stellar wind properties from the ultraviolet spectra. The following results are obtained:

ζ Puppis. (i) The effective temperature obtained from the analysis of optical hydrogen and helium absorption lines is confirmed, however, the gravity is larger by 0.1 dex. (ii) A solar abundance of iron yields a reasonable fit of the rich Fe IV and V spectra. The abundances of carbon, nitrogen and oxygen indicate that the atmosphere is mixed with CNO-burned material. (iii) A mass-loss rate of 5.1 $10^{-6} M_\odot$ yr^{-1} resulting from a self-consistent wind model gives the best fit to the UV-spectrum. In this model helium recombines from He^{++} to He^{+} in the outer wind layers as a result of the high wind density and photospheric line blocking in the wavelength region of the He II resonance line.

Melnick 42. (i) The HST UV spectrum indicates a higher effective temperature than found by Heap et al. (1991) from the analysis of the optical lines. The stellar parameters that lead to an optimum fit of the UV-spectrum are: $T_{\rm eff}$ = 50 500 K, $\log g = 3.785$ (cgs), $R/R_\odot = 26$, $M/M_\odot = 150$, $\log(L/L_\odot) = 6.6$. Melnick 42 is thus the most massive and most luminous star known. (ii) The mass-loss rate is 3 $10^{-5} M_\odot$ yr^{-1} with and uncertainty of 50%. This value is in agreement with the observed emission strength of Hα and He II 4686. (iii) The difference in $T_{\rm eff}$ relative to Heap et al. (1991) is attributed to the effect of the strong stellar wind and its influence on the formation of the optical hydrogen and helium lines. (iv) The abundance of all elements (including C, N, O and Fe) is reduced relative to the Sun by a factor of four.

Key words: stars: atmospheres – stars: fundamental parameters – stars: mass loss – atomic data – stars: individual: ζ Pup – Melnick 42

1. Introduction

The ultraviolet spectra of O-stars with their thousands of spectral lines provide a wealth of astrophysically important information about stellar parameters and abundances. However, although high resolution UV spectra of massive O-stars have been available since the seventies (Copernicus, IUE), the theoretical tools to extract the full information contained quantitatively have not been developed sufficiently. In practice, the quantitative analysis of UV O-star spectra concentrates on a few strong stellar wind lines and all the other lines (in particular the rich spectrum of iron group elements in ionization stages IV, V, VI) are ignored.

There are two reasons for this unsatisfactory status of the theory. First, the simplifying assumption of LTE fails completely in O-star atmospheres because of the intense radiation field and, thus, a NLTE treatment of all ions including the iron group elements is needed. As has become evident during the past decade, such NLTE calculations, if they are to be used for a quantitative comparison with observations, require very detailed and sophisticated model

---

Send offprint requests to: A.W.A. Pauldrach atoms with a large number of energy levels and transitions and with sufficiently accurate atomic data. Second, the UV line spectrum is strongly affected by the presence of stellar winds. This is true not only for the few strong resonance lines that exhibit P-Cygni profiles but also for the many weak absorption lines observed (see Kudritzki 1992). In consequence, a hydrodynamic model atmosphere treatment that includes the effects of stellar winds is needed for theoretical spectrum synthesis calculations in the ultraviolet.

The intention of this paper is to present a first step towards fully quantitative UV-spectroscopy of massive O-stars based on NLTE radiation driven wind models. For this purpose, the calculations of stationary radiation driven wind models as outlined in previous papers of this series [Pauldrach et al. 1986 (Paper I); Paudrach 1987 (Paper III); Pauldrach et al. 1990 (Paper VII); Pauldrach et al. 1989 (Paper IX)] have been improved significantly (see Sect. 2). For the most important ions detailed model atoms with more accurate atomic data are used. The emission of shocks arising from the non-stationary, unstable behaviour of radiation driven winds is now additionally taken into account in the rate equations and the radiative transfer (for observational evidence of non-stationarity see for example Henrichs 1988; for theoretical investigations see Lucy 1982; Krolik & Raymond 1985; Owocki et al. 1988; Mac Farlane & Cassinelli 1989; Cassinelli & Olson 1979) and the effects of EUV line blocking on the ionization and excitation of levels are discussed and simulated (see also Papers IX and VII).

These wind models are then used to calculate synthetic high resolution spectra of O-stars covering the full observable UV spectral range. A comparison with observed spectra of two Of-stars (ζ Puppis in the Galaxy and Melnick 42 in the LMC) is then carried out to obtain physical constraints on the properties of stellar winds but also to develop diagnostic tools to determine abundances together with stellar parameters (Sect. 3).

2. The calculations

The basis of our model calculation is the concept of stationary radiation driven winds as developed in Papers I, III, VII, and IX (see Sect. 1). Before we describe these calculations in more detail it is important to recognize that the restriction to stationarity might be a severe limitation. There is a vast amount of data now available that demonstrate the presence of variability in O-star spectra (Lamers et al. 1982; Prinja & Howarth 1986; Henrichs 1986; Ebbets 1982; Bieging et al. 1989). On the other hand, the amplitudes of detected line profile variations are normally small which admits the possibility that stationary models are capable of providing a good description of the time averaged spectra of O-stars. We note, however, that this conclusion appears to be in conflict with recent non-stationary calculations (Owocki et al. 1988) of radiation driven wind models that show large density contrasts between dense shells in the wind and almost empty intershell regions. But we also note that at the moment these calculations still make use of several severe approximations which might lead to artificially high density contrasts such as the assumptions on the amplitudes of the perturbation at the inner boundary, the neglect of the energy equation for the treatment of shocks, the use of a simplified radiative line force and the restriction to spherical geometry. Since it will take years before we will be in a position to drop these approximations, we feel that it is worthwhile to continue with the stationary approach and to improve its inherent physics. The detailed comparison with the observations will then demonstrate its reliability.

Figure 1 gives an overview of the status of the theory as outlined in Papers I, III, VII, and IX. To calculate a wind model, the stellar parameters $T_{\rm eff}$ (effective temperature), $\log g$ (logarithm of photospheric gravitational acceleration), R_* (photospheric radius defined at a pre-specified Thomson optical depth) and Z (abundances) have to be specified. Then the stationary hydrodynamic equations are solved in spherical symmetry (r is the radial coordinate, ρ the mass density, v the velocity, p the gas pressure and $\dot{M}$ the rate of mass-loss). The crucial term is the radiative acceleration $g_{\rm rad}$ that has contributions from continuous absorption and scattering ($g_{\rm cont}$) and the line absorption. The calculation of the line acceleration is performed by summing the contributions of more than 200 000 lines (see Sect. 2.6). For each line the oscillator strengths $f_{\rm lu}$, the statistical weights $g_{\rm l}$, $g_{\rm u}$ and the occupation numbers $n_{\rm l}$, $n_{\rm u}$ of the lower and upper level enter together with the frequency and angle integral over the specific intensity I_ν and the line broadening function φ_ν accounting for the Doppler effect.

The occupation numbers are determined by the rate equations containing collisional (C_{ij}) and radiative (R_{ij}) transiton rates. Details of the atomic models and the physical processes taken into account will be discussed in Sect. 2.1–2.4. It is important to note that the hydrodynamical equations are coupled directly with the rate equations. The velocity field enters into the radiative rates while the density is important for the collisional rates and the equation of particle conservation. On the other hand, the occupation numbers are crucial for the hydrodynamics since the radiative line acceleration dominates the equation of motion.

In addition, the radiation field determined by the equation of transfer is coupled with the hydrodynamics (radiative line acceleration) and the rate equations (radiative rates). Details of the calculation of the radiation field are discussed in Sects. 2.2–2.4 and 2.7.

The temperature is, in principle, determined by the energy equation, which depends on h, the free enthalpy, $H^{\rm rad}$ the radiative flux and $H^{\rm diss}$ the energy flux generated by dissipative processes. The simplifications for the temperature structure used in our code are discussed in Sect. 2.5.

The iterative solution of the total system of equations then yields the hydrodynamic structure of the wind (including mass-loss rate and terminal velocity) together with syn-

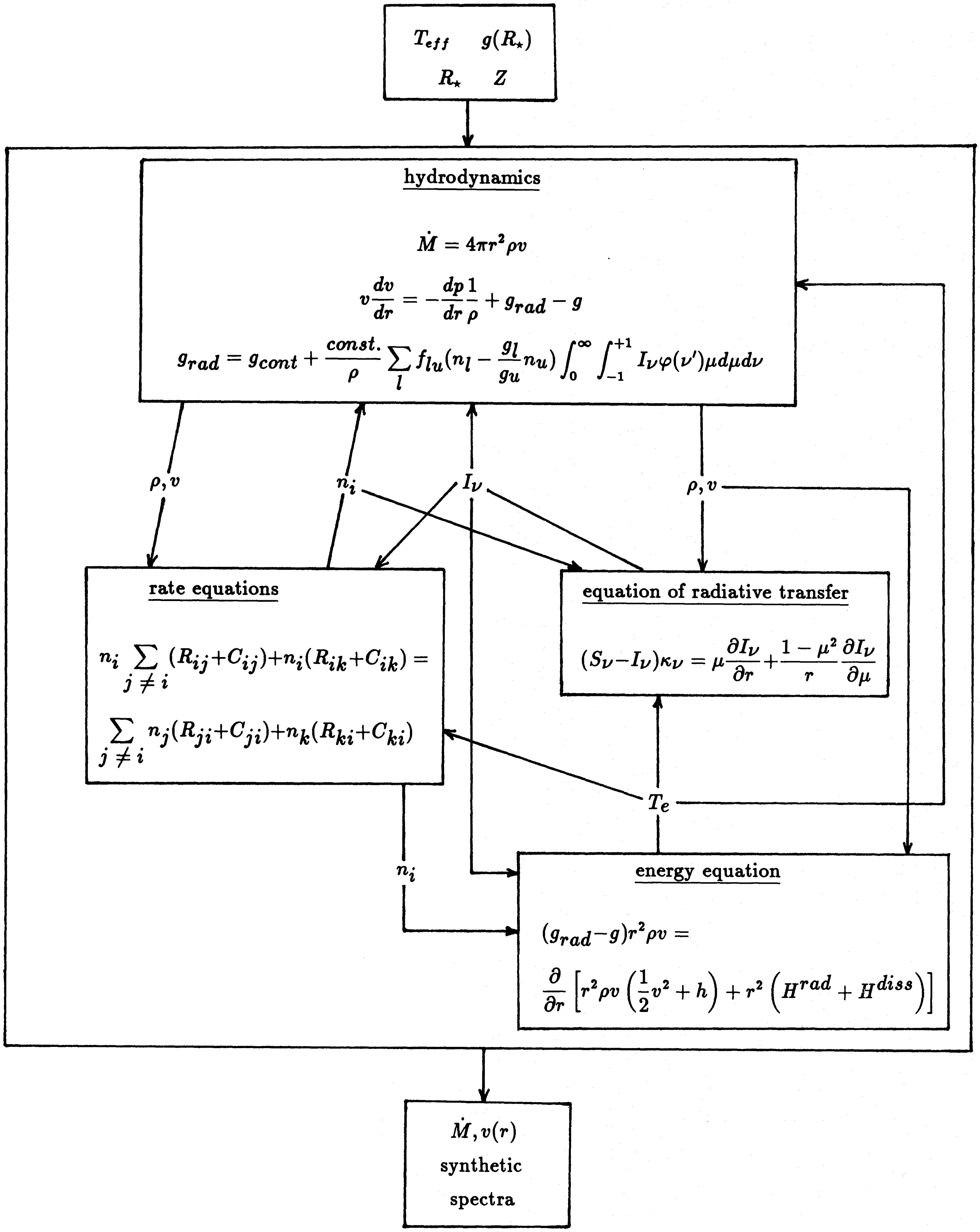

Fig 1. Schematic sketch of the non-linear system of integro-differential equations that form the basis of stationary radiation driven wind theory (the first box shows the input, effective temperature $T_{\rm eff}$, abundances Z, stellar radius R_*, and surface gravity g, required for a model calculation; the second shows the equations of hydrodynamics where special attention is drawn to the expression for the radiative line acceleration $g_{\rm rad}$; the third, fourth and fifth boxes shows the rate equations together with the line and continuum radiative transfer and the energy balance. They form the basis of spherically extended NLTE calculations; the sixth box shows the output of the computations, mass loss rate $\dot{M}$, terminal velocity and synthetic spectra which when compared to the observed spectra yield information about the stellar parameters, abundances and plasma conditions. Most of the symbols are explained in the text, for those remaining we refer to earlier papers of this series (e.g. Papers I, III and IV or to the book by Mihalas 1978)

thetic spectra that can be compared with observations (see Sect. 3).

In the following subsections we discuss the status quo and the improvements in the different areas sketched in Fig. 1.

2.1. *Atomic models and rate equations*

NLTE spectrum synthesis requires the use of realistic atomic models in the rate equations (for references, see Kudritzki & Hummer 1990). In our previous calculations we concentrated mainly on the principle hydrodynamical effects of line driven winds and used simplified atomic models and very approximate atomic data to be able to handle the contribution of some 100 000 line of 26 elements in full NLTE for the first time (Papers III, VII, IX).

For our new generation of models to be used for detailed spectrum synthesis the atomic data of the most important ionization stages have been replaced by more accurate values. In addition, more energy levels and transitions were included and higher ionization stages were added. In total, the following ions are affected:

H I; He I, II; C III IV, V; N III, IV, V, VI; O IV, V, VI; Si IV; P V. VI; S VII; Ar VI, VII, VIII; Fe IV, V, VI, VII, VIII; Ni V, VI, VII, VIII.

To implement these improvements we utilised the program SUPERSTRUCTURE (Eissner et al. 1974; Nussbaumer & Storey 1978), which uses the configuration interaction approximation to determine wavefunctions and radiative data first in LS-coupling. The wavefunction for each term is expanded in terms of a basis set of Slater determinants

$$\Phi = \sum_i c_i \, \Phi_i \, .$$

The one-electron orbitals appearing in the latter are varied so that the sum of the energies of the terms of interest is a minimum, i.e. the variational principle is invoked. The energies and coefficients c_i are found by a standard diagonalization of the non-relativistic N-electron Hamiltonian. Given these optimum wave-functions relativistic energies and oscillator strengths are obtained via a perturbation theory calculation involving the Breit–Pauli Hamiltonian. This means that the method is limited to systems where the relativistic effects are not too large. For the ions of interest here ($Z < 30$) this is always the case.

SUPERSTRUCTURE is also used to calculate the transition probabilities for the inclusion of dielectronic recombination in the approximation described by Mihalas & Hummer (1973). It should be noted that the wind conditions of O-stars require the inclusion not only of the individual transition probabilities of each stabilizing downward transition, but also of the inverse process, which is non-negligible.

For the calculation of the bound–free radiative rates, more accurate, e.g. Coulomb approximation, photoionization cross-sections fitted to the Seaton formula (1958) have been included but only for the lowest 5–10 levels per ionisation stage. For the other levels we still use the Gould (1978) formula to calculate the threshold value (see Paper III). Our approximate procedure for the calculation of the collisional rates has been improved for those cases where the transition is decisive for the level populations. For these cases, the data were taken, where possible from the compilation of Pradhan & Gallagher (1985). Examples of the new atomic data sets for some important ions used in our calculations are given in Fig. 2 and Table 1.

In summary, the whole set of rate equations now comprises 4228 energy levels in 142 ionisation stages of 26 elements with 14 783 bound–bound and 4341 bound–free transitions. The rate equations are solved at up to 41 depths points distributed over the entire atmosphere including the deeper subsonic region.

2.2. *Radiative transition probabilities*

For the calculation of the radiative bound–bound transition probabilities R_{ij} the Sobolev-approximation is used in the entire atmosphere. We note that this might be a poor approximation in the subsonic region in the atmospheric layers where the continuum is formed. However, at the moment this is still the simplest way to take the contribution of many ions in many line transitions into account simultaneously. Improvements such as the Sobolev plus continuum method (Hummer & Rybicki 1985; Puls & Hummer 1988) or the comoving frame method (for applications in stellar wind dynamics, see Puls 1987) are presently being implemented.

Usually, in NLTE calculations with complex model atoms population inversions that lead to negative line opacities are frequently encountered. This is also the case for O-star stellar winds, particularly for high levels and infrared transitions, where the population of the corresponding upper and lower levels is frequently dominated by other transitions to these levels. It is a common procedure either to cancel such transitions from the rate equations or to damp the contribution of the stimulated emission.

However, an inspection of the equation of radiative transfer reveals that the case of inversion $[\Delta N = (g_\mathrm{u}/g_\mathrm{l})n_\mathrm{l} - n_\mathrm{u} < 0]$ and even the case of $\Delta N = 0$ can also be treated in the framework of the Sobolev approximation. With the normal definition of the Sobolev optical depth (τ_s) and the source function S_l (negative for $\Delta N < 0!$), the mean line intensity is then given by

$$\bar{J} = \beta_\mathrm{c} I_\mathrm{c} + (1-\beta) S_\mathrm{l} = \beta_\mathrm{c} I_\mathrm{c} + |S_\mathrm{l}|\,(\beta - 1)\,,$$

where

$$\beta, (\beta_\mathrm{c}) = \frac{1}{2} \int_{-1,(\mu_\mathrm{c})}^{1} \frac{1-\mathrm{e}^{-\tau_\mathrm{s}}}{\tau_\mathrm{s}} \, \mathrm{d}\mu$$

$$= \frac{1}{2} \int_{-1,(\mu_\mathrm{c})}^{1} \frac{\mathrm{e}^{|\tau_\mathrm{s}|} - 1}{|\tau_\mathrm{s}|} \, \mathrm{d}\mu$$

Fig. 2. Grotrian diagrams of the atomic models given in Table 1

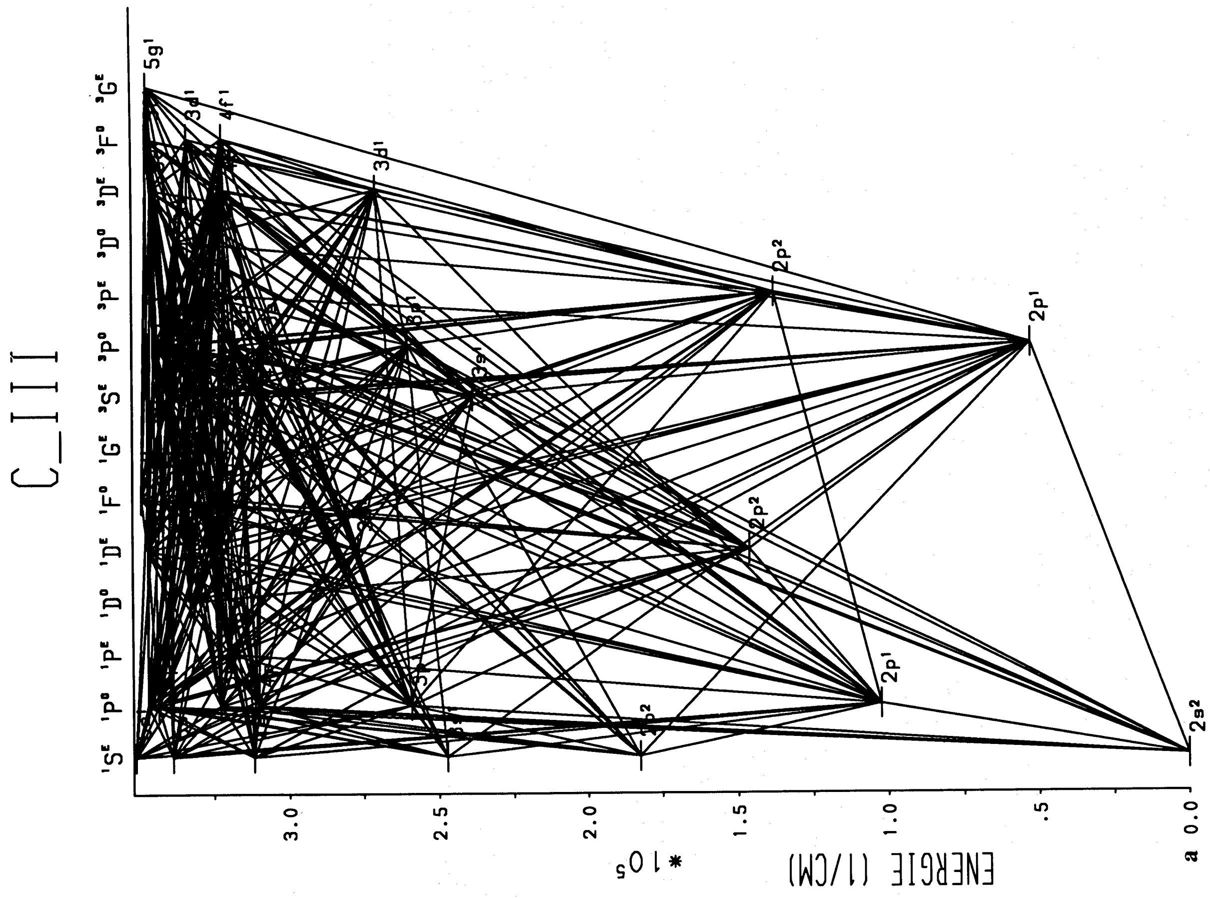

Fig. 2a. C III. Note that N IV and O V belong to the same isoelectronic sequence

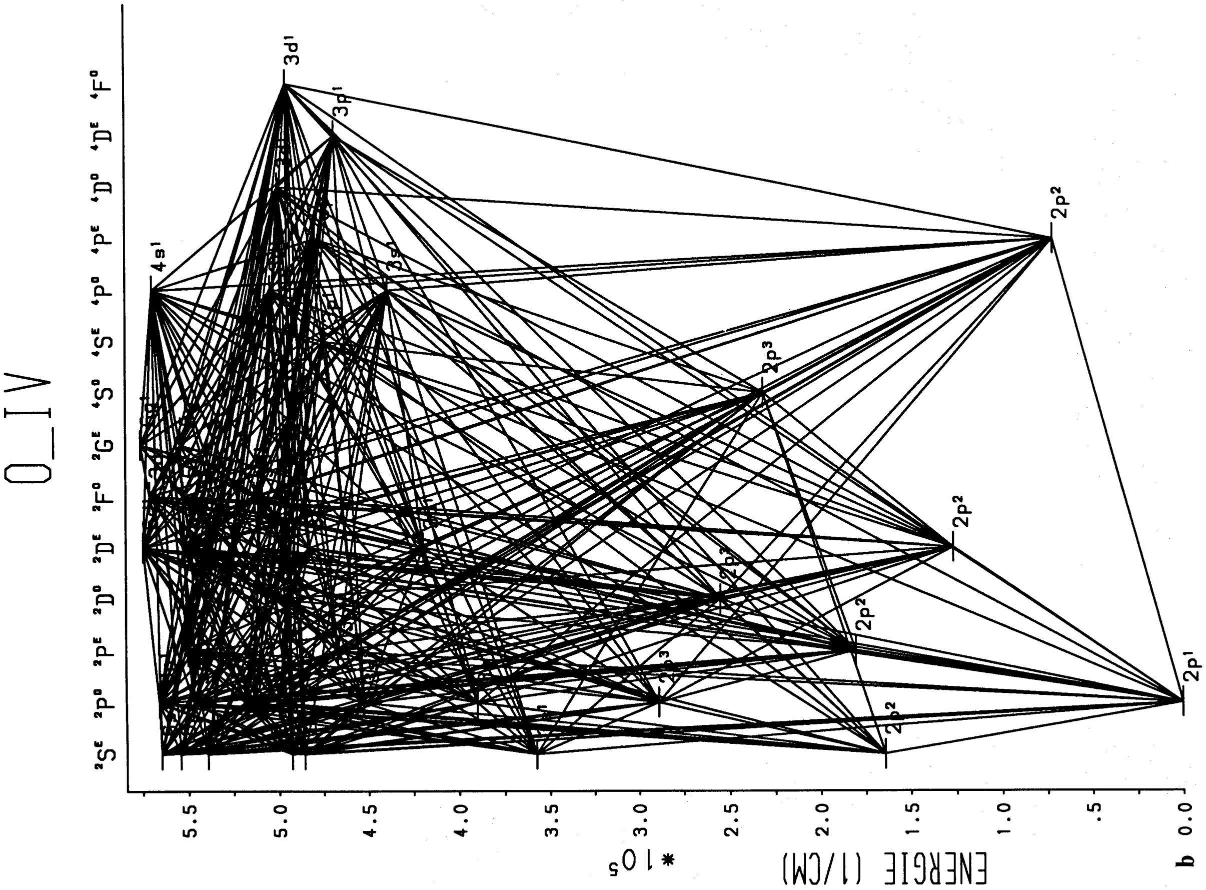

Fig. 2b. O IV. Note that N III belongs to the same isoelectronic sequence

Fig. 2 (continued)

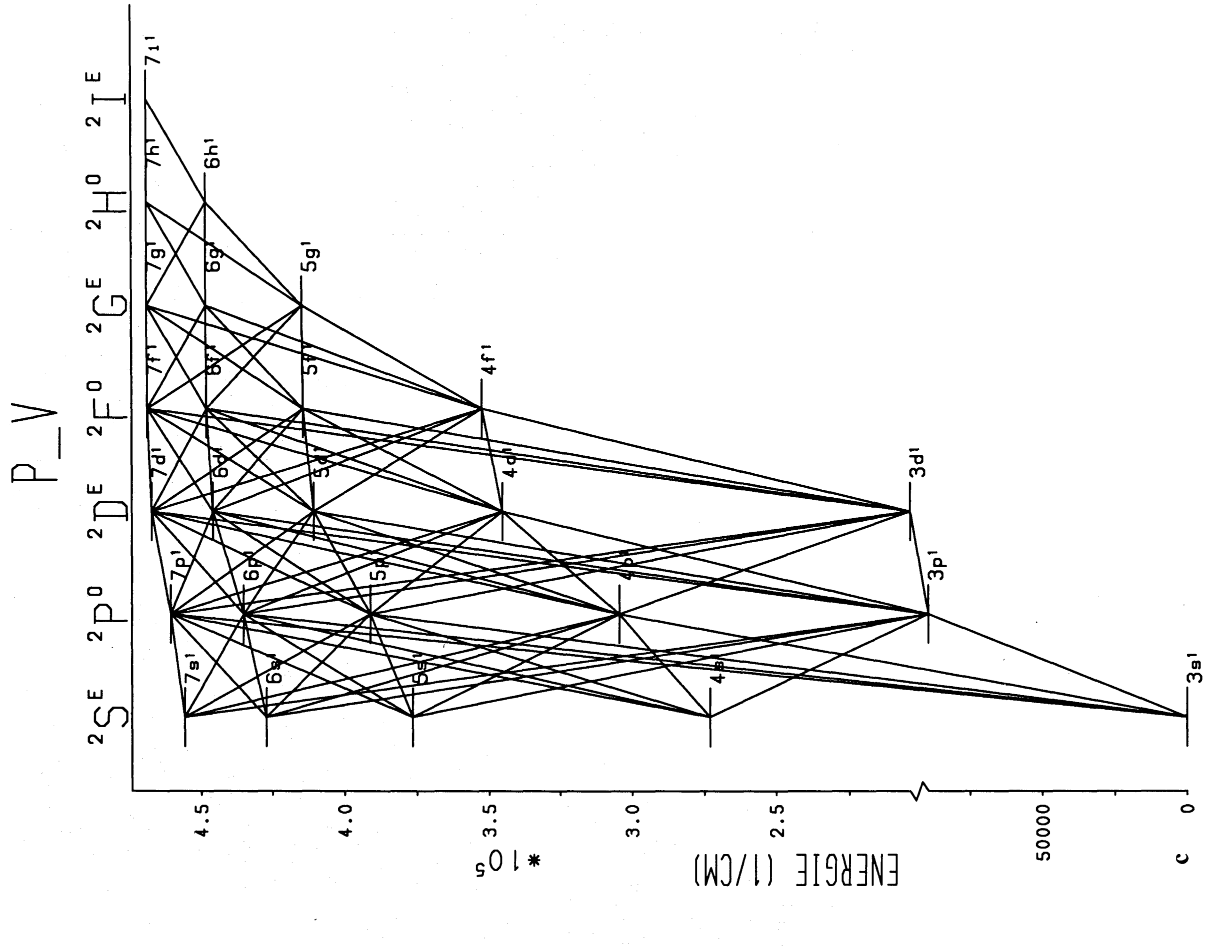

Fig. 2c. P V. Note that Si IV belongs to the same isoelectronic sequence

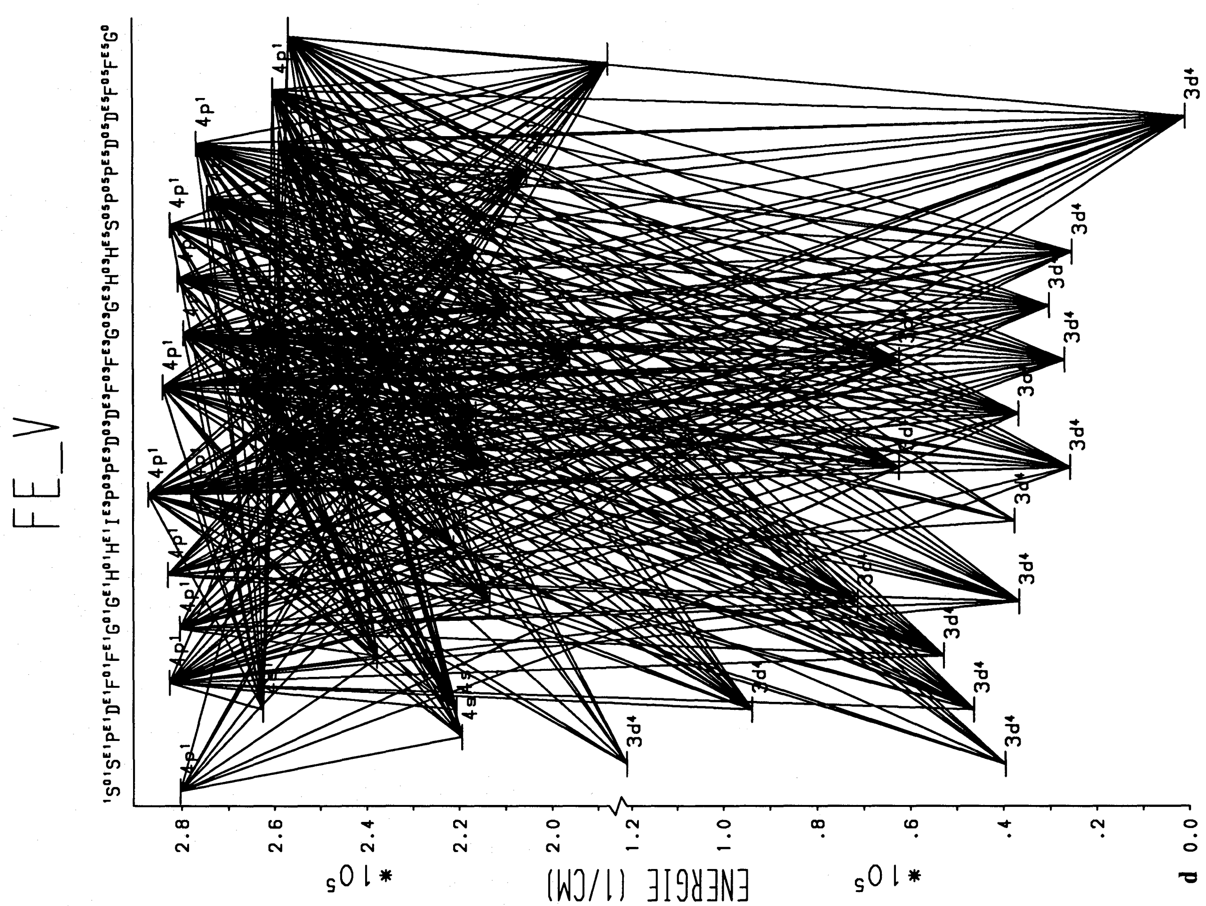

Fig. 2d. Fe V

Table 1. Examples of the atomic structure of some ionization stages considered in the calculations. Columns 1 and 2 give the level excitation number and the term disignation of each level respectively. In columns 3–5 the statistical weights, the excitation energy and the photoionization energy are given, respectively. Columns 6–8 give the values of α, β and s used in the Seaton formula to describe the photoionization cross section (see text)

Element C III							
	Energy Level			Photoionisation			
Level	Term	Stat. Weight	Excit.-energy (1/cm)	Ion.-energy (1/cm)	α	β	s
1	2s^2 ^{1}S^e	1	0.0	386241.0	1.430	1.00	1.50
2	2p ^{3}P^o	9	52419.4	333821.6	2.110	2.00	2.00
3	2p ^{1}P^o	3	102352.0	283889.0	2.130	–0.10	1.5
4	2p^2 ^{3}P^e	9	137477.7	313319.1	3.980	2.00	2.00
5	2p^2 ^{1}D^e	5	145876.1	304920.7	3.190	1.00	2.00
6	2p^2 ^{1}S^e	1	182519.9	268276.9	2.950	1.00	2.00
7	3s ^{3}S^e	3	238213.0	148028.0	0.890	2.00	2.00
8	3s ^{1}S^e	1	247170.3	139070.7	1.530	1.00	1.50
9	3p ^{1}P^o	3	258931.3	127309.7	2.970	1.00	1.50
10	3p ^{3}P^o	9	259717.8	126523.2	2.720	2.00	2.00
11	3d ^{3}D^e	15	270013.0	116228.0	3.190	2.00	2.00
12	3d ^{1}D^e	5	276482.9	109758.1	2.080	1.00	3.50
13	3s′ ^{3}P^o	9	308283.3	142513.5	0.171	2.00	2.00
14	4s ^{3}S^e	3	309457.2	76783.8	0.132	2.00	2.00
15	4p ^{3}P^o	3	310006.3	76234.7	0.133	2.00	2.00
16	4s ^{1}S^e	1	311721.5	74519.5	0.045	2.00	2.00
17	4p ^{1}P^o	9	317798.9	68442.1	0.445	2.00	2.00
18	3p′ ^{1}P^e	3	319720.3	131076.5	0.062	2.00	2.00
19	4d ^{3}D^e	15	321434.5	64806.5	0.784	2.00	2.00
20	4f ^{3}F^o	21	322011.8	64229.2	1.108	2.00	2.00
21	4f ^{1}F^o	7	322702.0	63539.0	0.373	2.00	2.00
22	3s′ ^{1}P^o	3	322702.0	128094.8	0.063	2.00	2.00
23	3p′ ^{3}D^e	15	323114.7	127682.1	0.317	2.00	2.00
24	4d ^{1}D^e	5	324212.5	62028.5	0.273	2.00	2.00
25	3p′ ^{3}S^e	3	327278.3	123518.5	0.066	2.00	2.00
26	3p′ ^{3}P^e	9	329724.8	121072.0	0.201	2.00	2.00
27	3d′ ^{1}D^o	5	332691.3	118105.5	0.114	2.00	2.00
28	3p′ ^{1}D^e	5	333118.2	117678.6	0.115	2.00	2.00
29	3d′ ^{3}F^o	21	333421.0	117375.8	0.483	2.00	2.00
30	3d′ ^{3}D^o	15	337675.2	113121.6	0.358	2.00	2.00
31	5s ^{1}S^e	1	338514.3	47726.7	0.036	2.00	2.00
32	5s ^{3}S^e	3	339934.7	46306.3	0.112	2.00	2.00
33	3d′ ^{3}P^o	9	340114.8	110682.0	0.220	2.00	2.00
34	5f ^{1}F^o	7	341370.9	44870.1	0.271	2.00	2.00
35	5p ^{1}P^o	3	343258.0	42983.0	0.121	2.00	2.00
36	5p ^{3}P^o	9	344234.7	42006.3	0.372	2.00	2.00
37	3p′ ^{1}S^e	1	345095.4	105701.4	0.025	2.00	2.00
38	5d ^{3}D^e	15	345496.9	40744.1	0.639	2.00	2.00
39	5g ^{1}G^e	9	346579.3	39661.7	0.394	2.00	2.00
40	5g ^{3}G^e	27	346579.3	39661.7	1.181	2.00	2.00
41	5d ^{1}D^e	5	346658.3	39582.7	0.219	2.00	2.00
42	3d′ ^{1}P^o	3	346712.7	104084.1	0.077	2.00	2.00
43	5f ^{3}F^o	21	347153.9	39087.1	0.932	2.00	2.00
44	3d′ ^{1}F^o	7	348860.0	101936.8	0.184	2.00	2.00
45	6s ^{1}S^e	1	350921.8	35319.2	0.071	2.00	2.00
46	6s ^{3}S^e	3	354858.0	31383.0	0.238	2.00	2.00
47	6p ^{3}P^o	9	357050.7	29190.3	0.768	2.00	2.00
48	6p ^{1}P^o	3	357109.7	29131.3	0.257	2.00	2.00
49	6d ^{3}D^e	15	357998.0	28243.0	1.324	2.00	2.00
50	6g ^{3}G^e	27	358692.3	27548.7	2.442	2.00	2.00

Table 1b. O IV

Element O IV							
	Energy Level			Photoionisation			
Level	Term	Stat. Weight	Excit.-energy (1/cm)	Ion.-energy (1/cm)	α	β	s
1	2p ^{2}P^o	6	257.3	624124.7	1.090	0.80	3.00
2	2p^2 ^{4}P^e	12	71641.1	634974.8	2.170	2.00	2.00
3	2p^2 ^{2}D^e	10	126941.9	579674.0 656237.8	2.230 2.110	2.00 2.00	2.00 2.00
4	2p^2 ^{2}S^e	2	164366.4	542249.5 618813.3	2.160 2.200	2.00 2.00	2.00 2.00
5	2p^2 ^{2}P^e	6	180643.1	525972.8 602536.6	2.290 2.180	2.00 2.00	2.00 2.00
6	2p^3 ^{4}S^o	4	231537.5	606594.7	2.200	2.00	2.00
7	2p^3 ^{2}D^o	10	255167.5	582964.7 600935.9	2.200 2.200	2.00 2.00	2.00 2.00
8	2p^3 ^{2}P^o	6	289020.8	549111.4 567082.6 623271.5	2.200 2.200 2.200	2.00 2.00 2.00	2.00 2.00 2.00
9	3s ^{2}S^e	2	357614.3	266767.7	0.120	2.00	2.00
10	3p ^{2}P^o	6	390219.1	234162.9	0.412	2.00	2.00
11	3d ^{2}D^e	10	419543.9	204838.1	0.784	2.00	2.00
12	3s′ ^{4}P^o	12	439084.9	267531.0	0.065	2.00	2.00
13	3s′ ^{2}P^o	6	452983.2	253632.7	0.034	2.00	2.00
14	3p′ ^{2}P^e	6	467306.4	239309.5	0.036	2.00	2.00
15	3p′ ^{4}D^e	20	468585.9	238030.0	0.121	2.00	2.00
16	3p′ ^{4}S^e	4	474478.1	232137.8	0.025	2.00	2.00
17	3p′ ^{4}P^e	12	478991.7	227624.1	0.076	2.00	2.00
18	3p′ ^{2}D^e	10	482819.4	223796.5	0.065	2.00	2.00
19	4s ^{2}S^e	2	485821.7	138560.3	0.098	2.00	2.00
20	3p′ ^{2}S^e	2	492890.9	213725.0	0.014	2.00	2.00
21	3d′ ^{4}F^o	28	495362.8	211253.1	0.192	2.00	2.00
22	3d′ ^{4}D^o	20	499851.4	206764.4	0.140	2.00	2.00
23	4p ^{2}P^o	6	500023.5	124358.5	0.327	2.00	2.00
24	3d′ ^{2}D^o	10	501542.3	205073.5	0.070	2.00	2.00
25	3d′ ^{4}P^o	12	504164.5	202451.3	0.086	2.00	2.00
26	4d ^{2}D^e	10	510572.3	113809.7	0.595	2.00	2.00
27	3d′ ^{2}F^o	14	510877.6	195738.2	0.103	2.00	2.00
28	4f ^{2}F^o	14	513193.5	111188.5	0.853	2.00	2.00
29	3d′ ^{2}P^o	6	514270.7	192345.2	0.045	2.00	2.00
30	3s′ ^{2}P^o	6	518705.7	187910.2	0.046	2.00	2.00
31	5s ^{2}S^e	2	539368.0	85014.0	0.082	2.00	2.00
32	5p ^{2}P^o	6	546813.6	77568.4	0.268	2.00	2.00
33	3p′ ^{2}D^e	10	547343.4	159272.5	0.091	2.00	2.00
34	3p′ ^{2}P^e	6	549834.0	156781.9	0.055	2.00	2.00
35	5d ^{2}D^e	10	552031.2	72350.8	0.479	2.00	2.00
36	5f ^{2}F^o	14	552495.1	71886.9	0.676	2.00	2.00
37	5g ^{2}G^e	18	554001.6	70380.4	0.887	2.00	2.00
38	3p′ ^{2}S^e	2	554464.0	152151.9	0.019	2.00	2.00
39	6s ^{2}S^e	2	564662.2	59719.8	0.134	2.00	2.00
40	6p ^{2}P^o	6	565785.8	58596.2	0.411	2.00	2.00
41	4s′ ^{4}P^o	12	569137.0	137478.9	1.577	2.00	2.00
42	3d′ ^{2}F^o	14	570796.6	135819.3	0.149	2.00	2.00
43	6d ^{2}D^e	10	574368.7	50013.3	0.803	2.00	2.00
44	6g ^{2}G^e	18	575507.4	48874.6	1.479	2.00	2.00

and

$$\tau_{\mathrm{s}} = \frac{\pi e^2}{m_{\mathrm{e}} c} f_{\mathrm{lu}} \left(n_{\mathrm{l}} - \frac{g_{\mathrm{l}}}{g_{\mathrm{u}}} n_{\mathrm{u}} \right) \frac{c}{\nu_0} \left[(1-\mu^2)\,\frac{v}{r} + \mu^2\,\frac{\mathrm{d}v}{\mathrm{d}r} \right]^{-1},$$

$$\mu_{\mathrm{c}} = \left[1 - \left(\frac{R_*}{r} \right)^2 \right]^{1/2}.$$

This approximation is frequently applied in the analysis of astrophysical masers in the presence of velocity fields. Langer & Watson (1984), for instance, have shown that the error introduced (in comparison to the exact solution) is of minor importance.

The radiative bound–free transition probabilities R_{ik} are obtained by a full solution of the spherical transfer equation which yields the continuous radiation field at up to 900 frequency points at every depth point including the deepest layers where the radiation is thermalized and the diffusion approximation is applicable. The continuous opacities include Thomson-scattering and the free–free contribution of all ions (subroutine provided by D.G. Hummer). In addition, the bound–free opacities of up to 100 ground and

Table 1c. P V

Element P V

	Energy Level			Photoionisation			
Level	Term	Stat. Weight	Excit.-energy (1/cm)	Ion.-energy (1/cm)	α	β	s
1	3s ^{2}S^e	2	0.0	524462.9	0.250	1.69	2.00
2	3p ^{2}P^o	6	89182.1	435280.8	0.221	2.00	2.00
3	3d ^{2}D^e	10	204203.2	320259.7	0.501	2.00	2.00
4	4s ^{2}S^e	2	272959.3	251503.6	0.054	2.00	2.00
5	4p ^{2}P^o	6	304350.5	220112.4	0.185	2.00	2.00
6	4d ^{2}D^e	10	345398.7	179064.2	0.378	2.00	2.00
7	4f ^{2}F^o	14	352594.2	171868.7	0.552	2.00	2.00
8	5s ^{2}S^e	2	376645.3	147817.6	0.047	2.00	2.00
9	5p ^{2}P^o	6	391207.3	133255.6	0.156	2.00	2.00
10	5d ^{2}D^e	10	410637.4	113825.5	0.305	2.00	2.00
11	5f ^{2}F^o	14	414467.7	109995.2	0.442	2.00	2.00
12	5g ^{2}G^e	18	414686.8	109776.1	0.569	2.00	2.00
13	6s ^{2}S^e	2	427185.4	97277.5	0.041	2.00	2.00
14	6p ^{2}P^o	6	435097.9	89365.0	0.135	2.00	2.00
15	6d ^{2}D^e	10	445838.8	78624.1	0.255	2.00	2.00
16	6f ^{2}F^o	14	448090.2	76372.7	0.368	2.00	2.00
17	6g ^{2}G^e	18	448230.3	76232.6	0.474	2.00	2.00
18	6h ^{2}H^o	22	448250.3	76212.6	0.579	2.00	2.00
19	7s ^{2}S^e	2	455602.5	68860.4	0.037	2.00	2.00
20	7p ^{2}P^o	6	460371.4	64091.5	0.118	2.00	2.00
21	7d ^{2}D^e	10	466936.1	57526.8	0.220	2.00	2.00
22	7f ^{2}F^o	14	468363.5	56099.4	0.315	2.00	2.00
23	7g ^{2}G^e	18	468456.2	56006.7	0.406	2.00	2.00
24	7h ^{2}H^o	22	468469.5	55993.4	0.497	2.00	2.00
25	7i ^{2}I^e	26	468474.8	55988.1	0.587	2.00	2.00

Table 1d. Fe V

Element Fe V

	Energy Level				Photoionisation			
Level	Term		Stat. Weight	Excit.-energy (1/cm)	Ion.-energy (1/cm)	α	β	s
1	3d^4	^{5}D	25	787.2	609322.2 627401.1	0.477 0.200	2.00 2.00	2.00 2.00
2	3d^4	^{3}H	33	25265.1	584844.3 604685.2 612666.1 630063.6	0.300 0.135 0.390 0.075	2.00 2.00 2.00 2.00	2.00 2.00 2.00 2.00
3	3d^4	^{3}P2	9	25701.7	584407.6 602486.5 609646.0 611785.8 629627.0 655088.2	0.038 0.044 0.010 0.092 0.038 0.024	2.00 2.00 2.00 2.00 2.00 2.00	2.00 2.00 2.00 2.00 2.00 2.00
4	3d^4	^{3}F2	21	26879.3	583230.1 601308.9 603071.0 608468.5 610608.2 611051.8 628449.4 653910.6	0.153 0.038 0.061 0.003 0.214 0.075 0.010 0.010	2.00 2.00 2.00 2.00 2.00 2.00 2.00 2.00	2.00 2.00 2.00 2.00 2.00 2.00 2.00 2.00
5	3d^4	^{3}G	27	30176.8	579932.6 599773.5 607754.3 625151.9 650613.1	0.245 0.130 0.135 0.138 0.088	2.00 2.00 2.00 2.00 2.00	2.00 2.00 2.00 2.00 2.00
6	3d^4	^{1}G2	9	36586.3	593364.0	0.365	2.00	2.00
7	3d^4	^{3}D	15	36732.0	573377.4	0.189	2.00	2.00
8	3d^4	^{1}I	13	37511.7	592438.6	0.529	2.00	2.00
9	3d^4	^{1}S2	1	39633.4	597854.1	0.967	2.00	2.00
10	3d^4	^{1}D2	5	46291.2	583659.1	0.206	2.00	2.00
11	3d^4	^{1}F	7	52732.7	577217.6	0.292	2.00	2.00
12	3d^4	^{3}F1	21	62300.0	547809.4	0.277	2.00	2.00
13	3d^4	^{3}P1	9	62381.6	547727.8	0.119	2.00	2.00
14	3d^4	^{1}G1	9	71280.3	558670.0	0.388	2.00	2.00
15	3d^4	^{1}D1	5	93832.3	536118.0	0.225	2.00	2.00
16	3d^4	^{1}S1	1	121130.2	516357.3	1.120	2.00	2.00
17	3d^3(^{4}F)4s	^{5}F	35	187567.1	422542.2	0.054	2.00	2.00
18	3d^3(^{4}F)4s	^{3}F	21	196145.7	413963.7	0.033	2.00	2.00
19	3d^3(^{4}P)4s	^{5}P	15	205188.1	423000.1	0.097	2.00	2.00
20	3d^3(^{2}G)4s	^{3}G	27	209208.2	420742.1	0.116	2.00	2.00
21	3d^3(^{2}G)4s	^{1}G	9	213534.1	416416.2	0.039	2.00	2.00
22	3d^3(^{4}P)4s	^{3}P	9	213865.0	414323.2	0.113	2.00	2.00
23	3d^3(^{2}P)4s	^{3}P	9	214762.0	413426.2	0.007	2.00	2.00
24	3d^3(^{4}D2)4s	^{3}D	15	216412.5	421075.1	0.193	2.00	2.00
25	3d^3(^{2}H)4s	^{3}H	33	216941.5	420989.7	0.386	2.00	2.00
26	3d^3(^{2}P)4s	^{1}P	3	219486.9	415860.9	0.391	2.00	2.00
27	3d^3(^{2}D2)4s	^{1}D	5	220621.0	416866.5	0.065	2.00	2.00
28	3d^3(^{2}H)4s	^{1}H	11	221305.2	416626.0	0.130	2.00	2.00
29	3d^3(^{2}F)4s	^{3}F	21	233799.1	376310.3	0.036	2.00	2.00
30	3d^3(^{2}F)4s	^{1}F	7	237729.6	417599.1	0.519	2.00	2.00
31	3d^3(^{4}F)4p	^{5}G	45	256751.0	353358.4	0.083	2.00	2.00
32	3d^3(^{2}D1)4s	^{3}D	15	258566.0	378921.6	0.215	2.00	2.00
33	3d^3(^{4}F)4p	^{5}D	25	258832.0	351277.4	0.046	2.00	2.00
34	3d^3(^{4}F)4p	^{5}F	35	260172.9	349936.5	0.065	2.00	2.00
35	3d^3(^{4}F)4p	^{3}D	15	260686.7	349422.7	0.028	2.00	2.00
36	3d^3(^{4}D1)4s	^{1}D	5	262509.3	374978.2	0.072	2.00	2.00
37	3d^3(^{4}F)4p	^{3}G	27	264571.7	345537.7	0.051	2.00	2.00
38	3d^3(^{4}F)4p	^{3}F	21	267385.8	342723.6	0.040	2.00	2.00
39	3d^3(^{4}P)4p	^{5}P	15	274408.1	353780.1	0.116	2.00	2.00
40	3d^3(^{4}P)4p	^{5}D	25	276769.1	333340.3	0.049	2.00	2.00
41	3d^3(^{4}P)4p	^{3}P	9	278030.3	350158.0	0.094	2.00	2.00
42	3d^3(^{2}G)4p	^{3}G	27	279537.7	330571.7	0.053	2.00	2.00
43	3d^3(^{2}P)4p	^{1}S	1	280337.0	355010.8	0.153	2.00	2.00
44	3d^3(^{2}G)4p	^{1}G	9	280367.2	349583.1	0.047	2.00	2.00
45	3d^3(^{2}G)4p	^{3}H	33	280715.7	349234.6	0.295	2.00	2.00
46	3d^3(^{4}P)4p	^{5}S	5	282423.5	345764.7	0.040	2.00	2.00
47	3d^3(^{2}G)4p	^{1}F	7	282571.6	347378.7	0.036	2.00	2.00
48	3d^3(^{2}G)4p	^{1}H	11	282871.9	347078.4	0.057	2.00	2.00
49	3d^3(^{2}G)4p	^{3}F	21	283924.8	326184.6	0.074	2.00	2.00
50	3d^3(^{2}P)4p	^{3}P	9	287074.9	341113.4	0.113	2.00	2.00

excited levels of the most important ions. Moreover, as we will show in Sect. 2.4, the EUV radiation field provided by shock emission is taken into account approximately.

The continuous radiation field is also used to calculate the incident continuous intensity I_c at the frequency of each line transition needed in the Sobolev-approximation for the bound–bound radiative transition probabilities. I_c is either based on the local value of the intensity (optically thick case) or obtained from the emergent continuous Eddington-flux H_c (optically thin case) via the equation

$$I_c = 4\left(\frac{r_{\max}}{R_*}\right)^2 H_c(r_{\max}) .$$

where a value of $100R_*$ is assumed for $r_{\max}$.

According to our experience, a proper treatment of the ionization and, therefore of the bound–free radiative transitions is extremely important to obtain reliable occupation numbers and, therefore, a reliable hydrodynamical structure. In particular, the fact that for O-stars the continuum shortward of the He II edge at 228 Å reaches optically thickness unity far out in the wind has important consequences for the ionization and the dynamics (see also Papers III and IX).

2.3. EUV metal line blocking

For the calculation of bound–free ionization transition probabilities R_{ik}, incident continuum intensities I_c and the radiative acceleration $g_{\rm rad}$ the influence of line blocking due to metal ions in the spectral region between 228 and 911 Å is extremely important. This is demonstrated in Fig. 3, which shows the emergent flux of a conventional hydrostatic NLTE model atmosphere for which the metal line opacity has been included in LTE.

The treatment of the influence of all these metal lines in the entire sub- and supersonically expanding atmosphere down to the thermalization depth in the calculation of R_{ik} correctly is a tremendous and hitherto unsolved problem. It

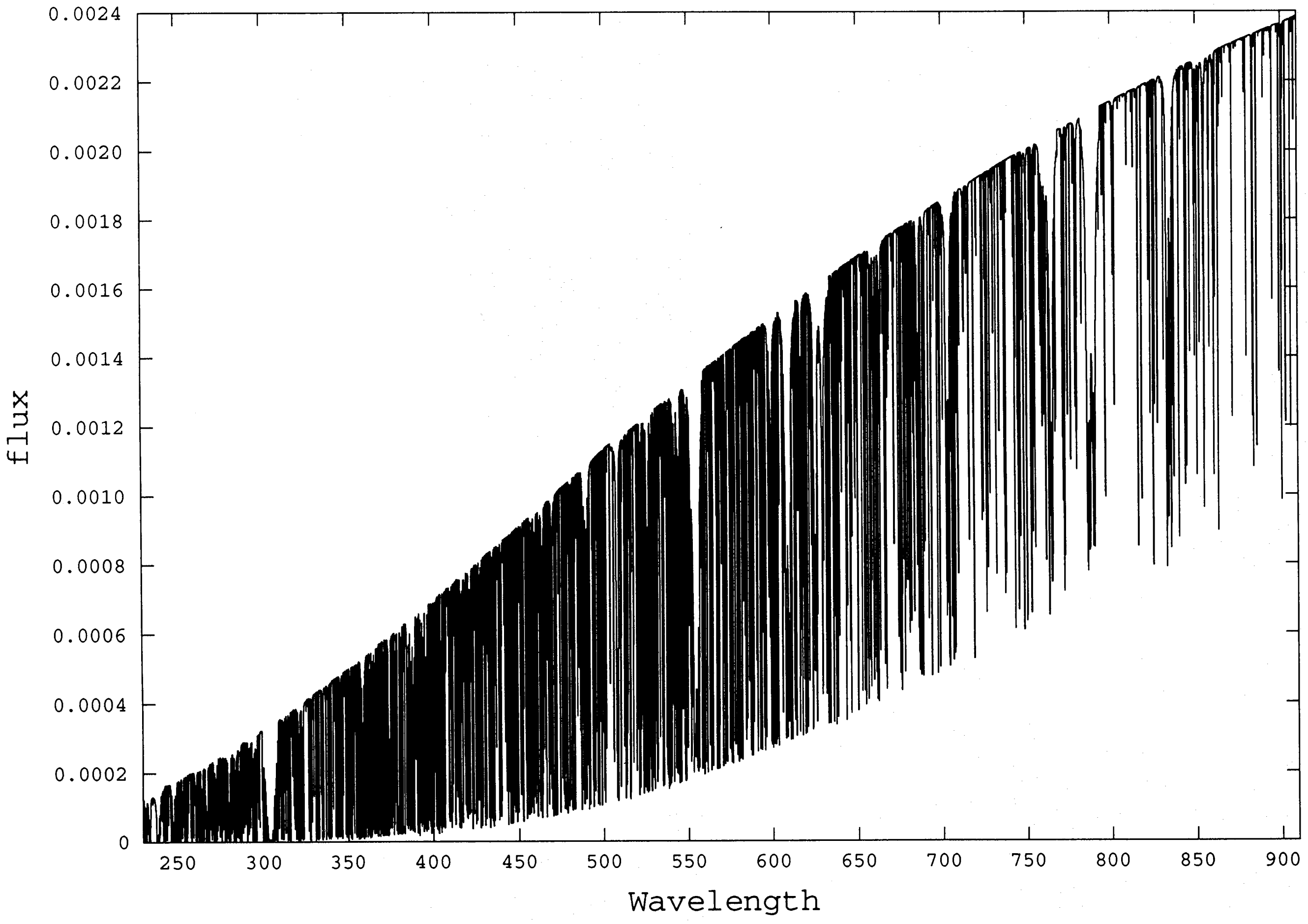

Fig. 3. The emergent flux ($\mathrm{erg\,cm^{-2}\,s\,Hz^{-1}}$) of a photospheric model of ζ-Pup in the range 227–911 Å. The influence of blocking due to line opacities is shown. This reduces the radiation field drastically in this frequency regime

requires the calculation of the mean intensity J_ν at every depth including not only the NLTE continuum opacities but also the NLTE opacities of all the overlapping, Doppler-shifted metal lines at all frequencies.

Several approximations have been used so far. Schmutz & Schaerer (1992) for instance did not solve the correct rate equations but approximated the ionization and excitation of metals by simple formulae to calculate the radiation field and g_{rad} down to thermalization depths. Puls (1987, Paper IV) performed a full solution of the rate equations including line overlaps in the bound–bound transition probabilities R_{ij} to investigate the influence of multi-line-effects on g_{rad}. However, he did not investigate the influence of these effects on the ionization transition probabilities R_{ik}. That these effects are indeed decisive was discussed qualitatively in Papers VII and IX. Moreover, for the radiative transfer the inner boundary was selected to be located above the depth of continuum formation (for 228 Å $< \lambda \le$ 911 Å) but below the sonic point and the emergent fluxes of photospheric hydrostatic models (either NLTE or Kurucz 1979) were used for the incident continuum radiation.

Our code has two options. In the first, we proceed as described in Sect. 2.2 but neglect the influence of the overlapping lines on R_{ik} and R_{ij} (or I_{c}, respectively).

For the radiative acceleration g_{rad} the contribution of all the lines is taken into account using NLTE occupation numbers but applying the Sobolev approximation for non-overlapping lines (see Sect. 2.6). Calculations done in this way usually yield too high ionization incompatible with the observation (see Sect. 3). However, since for the correct solution of the full problem, this option will be necessary.

The second option accounts for EUV line blocking in R_{ik} and I_{c} in an approximate way. In the subsonic region at velocities $v(r_i) \approx v_{\mathrm{sound}}/20$ (v_{sound} is the isothermal sound speed) a boundary r_i is introduced at which the optical thickness $\tau_\nu^{\mathrm{c}}(v_i) = \int_{r_i}^{\infty} \chi_\nu^{\mathrm{c}}\, \mathrm{d}r$ of the continuum is checked. If τ_ν^{c} is larger than unity (which is usually the case for $\lambda <$ 228 Å), we use the diffusion approximation based on χ_ν^{c} for the incident radiation field at r_i and solve the continuum transfer equation without line opacities for the calculation of R_{ik} and I_{c} (optically thick case, see Sect. 2.2).

If τ_ν^{c} is smaller than unity – usually for $\lambda >$ 228 Å, we adopt the emergent flux calculated from a hydrostatic model with the same T_{eff} and $\log g$ that includes metal line opacity as the incident radiation at r_i and solve the continuum transfer equation again to obtain the values of R_{ik} and I_{c} (optically thin, case, see Sect. 2.2). We normally use fluxes as in Fig. 3. However, for simplicity the incident radiation field is smoothed by introducing average radiation temperatures [defined by $4H_\nu = B_\nu\ (T_{\rm rad})$] over different frequency intervals. In addition, since the metal lines are treated in LTE in the hydrostatic model calculations – which is a poor approximation –, we have carried out experiments with $T_{\rm rad}(\nu)$ in the spectral region between 227 and 911 Å to investigate the sensitivity of individual ionization stages to this quantity (see Sect. 3, Fig. 6d).

We note here that this approximate treatment of EUV line blocking in the ionization and excitation radiative rates is the weakest point in our calculations. Fortunately, we have made significant progress in the correct treatment of the problem so that full NLTE calculations allowing an investigation of this approximation will be forthcoming within the next year.

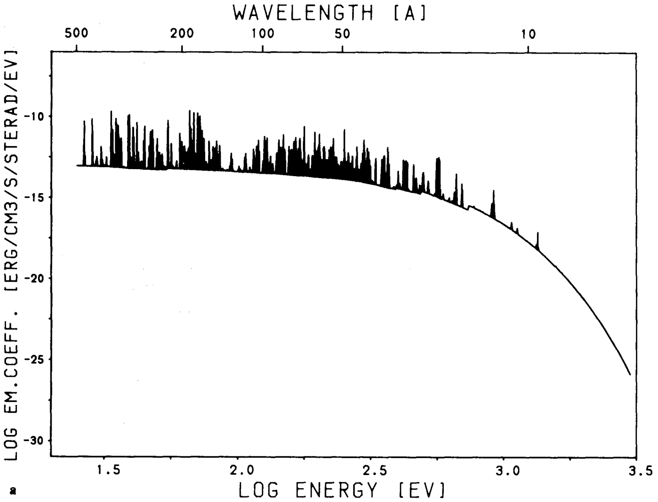

Fig. 4a. The emission coefficient $\varepsilon^{\rm s}_\nu$ resulting from a shock temperature of 1.1 10^6 K, corresponding to the observed microturbulent velocity of ζ-Pup (260 km $\rm s^{-1}$), and a particle density of 6.1 10^6 $\rm cm^{-3}$

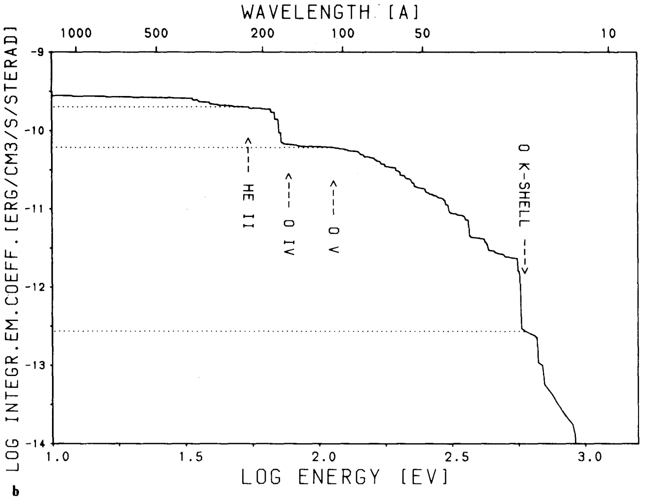

Fig. 4b. The energy integral over $\varepsilon^{\rm s}_\nu$ from Fig. 4a. It is shown that the radiative losses by shock heated matter influences almost the entire EUV part somewhat shortward of the He II edge

2.4. *Shock emission*

The X-ray emission of O-stars is now generally interpreted as radiation from shock instabilities in the stellar wind flow (Lucy & White 1980; Lucy 1982; Krolik & Raymond 1985; Owocki et al. 1988; Chen & White 1991). Recent results obtained with the ROSAT observatory (Hillier et al. 1993) strongly favour a model of randomly distributed shocks that build up a strong diffuse radiation field of which only a small fraction leaves the stellar wind to be observed as soft X-rays with $L_X/L \approx 10^{-7}$ (Chlebowski et al. 1989). In consequence, it is important to investigate whether this additional diffuse radiation field can affect the ionization of the stellar wind.

In principle, this is not a new idea. Soon after the detection of high ionization stages such as O VI, S VI, N V in stellar wind spectra (Snow & Morton 1976; Lamers & Morton 1976; Lamers & Rogerson 1978) such mechanisms were investigated (Cassinelli & Olson 1979; Olson & Castor 1981; Cassinelli & Swank 1983; Waldron 1984). However, only the effects of Auger-ionization, for instance from O IV to O VI, caused by X-rays were studied. As pointed out by Krolik & Raymond (1985) shock-heated matter radiates mostly in the ultraviolet and hence this is a severe restriction.

Figure 4a shows the emission coefficient $\varepsilon^{\rm s}_\nu$ of a shock with a typical temperature of 1.1 10^6 K calculated using the code developed by Raymond (1988), Cox & Raymond (1985), and Raymond & Smith (1977). The corresponding energy integral $F(E) = \int_E^\infty \varepsilon^{\rm s}_\nu\, {\rm d}E$ is given in Fig. 4b together with the edges for direct ionization of the outer shell electrons of He II(54 eV), O IV(77.4 eV), O V(113.9 eV) and the K-shell ionisation edge of oxygen (595 eV) (Daltabuit & Cox 1972). Since F(54 eV)/F(595 eV) $\approx$ 750 and F(113.9 eV)/F(595 eV) $\approx$ 230 for the assumed temperature of the shocks, we conclude that direct ionization, e.g. O IV to O V and O V to O VI, is at least at these temperatures the primary contribution of shock radiation to the ionization equilibrium. Since a large part of the O-star winds is optically thick at energies between 54 and 1000 eV, the inclusion of the shock radiation field into the rate equations requires a radiative transfer treatment that considers the emission $\varepsilon^{\rm s}_\nu$ of the shocks and the absorption $\chi^{\rm sw}_\nu$ and emission $\varepsilon^{\rm sw}_\nu$ of the ambient cool "standard" wind flow. To simplify these calculations we introduce a smoothed shock emission coefficient

$$\bar{\varepsilon}^{\rm s}_\nu = \frac{1}{E}\int_{E-\Delta E}^{E+\Delta E} \varepsilon^{\rm s}_\nu\, {\rm d}E\,, \qquad (1a)$$

with ΔE = 12.5 eV. Figure 5 demonstrates that for a reasonable range of shock temperatures and densities $\bar{\varepsilon}^{\rm s}_\nu$ can

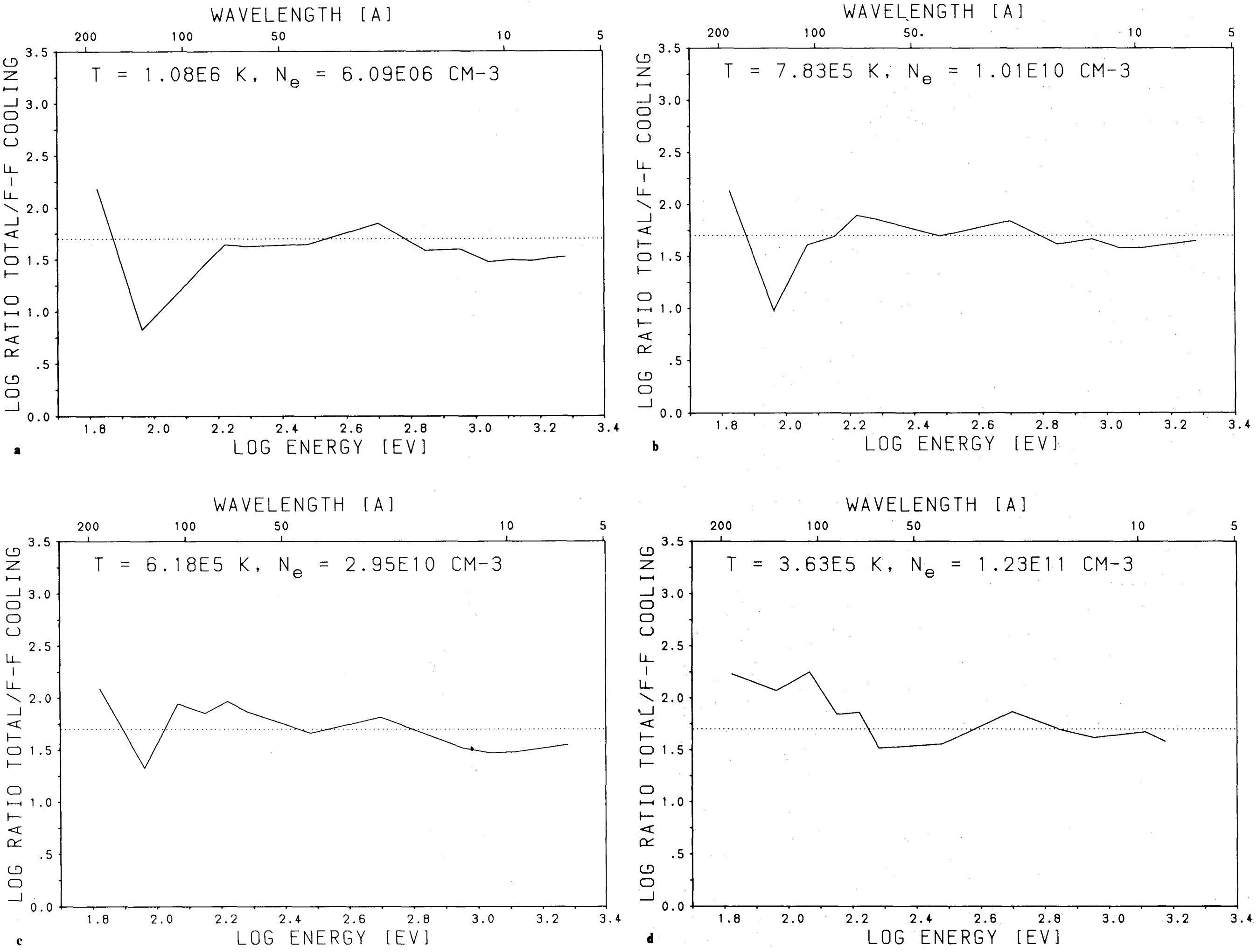

Fig. 5a–d. Ratio of the smoothed mean structure (integration intervals of 12.5 eV) of the shock emission coefficient, shown in Fig. 4, and the corresponding free–free emission coefficient. **a** shows this ratio for a shock temperature of 1.1 10^6 K in the X-ray and EUV region, **b, c** and **d** for shock temperatures of 7.8 10^5, 6.2 10^5 and 3.6 10^5 K, respectively, in the EUV band. The dotted line indicates that the calculated ratios can be approximated by a mean value of 50

be approximated by

$$\bar{\varepsilon}^{\mathrm{s}}_{\nu} \approx 50\ \varepsilon^{\mathrm{ff}}_{\nu}\,, \tag{1b}$$

where $\varepsilon^{\mathrm{ff}}_{\nu}$ is the hot gas free–free emission coefficient of hydrogen and helium calculated with the Gaunt factor equal to unity.

To calculate $\bar{\varepsilon}^{\mathrm{s}}_{\nu}$ via Eq. (1b) in the stellar wind we have to know the average density ρ_{s} and temperature T_{s} of the shocks as a function of the radius. Since there is no reliable theory available for these quantities, we take a very simple approach. For ρ_{s} we adopt a proportionality to the ambient unshocked gas, $\rho_{\mathrm{s}} = f^{1/2}\,\rho\,(r)$. Using Eq. (1b) and the equation of continuity for $\rho(r)$ we obtain

$$\bar{\varepsilon}^{\mathrm{s}}_{\nu} = f\left[6.15\;10^{8}\,\dot{M}^{2}\,\frac{1+2Y_{\mathrm{He}}}{1+4Y_{\mathrm{He}}}\right]\frac{1}{r^{4}v^{2}(T_{\mathrm{s}})^{1/2}}\;\mathrm{e}^{-h\nu/kT_{\mathrm{s}}}\,, \tag{1c}$$

with $Y_{\mathrm{He}} = n_{\mathrm{He}}/n_{\mathrm{H}}$; the number fraction of He. The "filling factor" f will be obtained from the observed X-ray flux or from an ad hoc adopted ratio of L_x/L_* (see below).

The immediate post shock temperature T_{s} is given by the Rankine– Hugoniot relation

$$T_{\mathrm{s}}(r) = \frac{3}{16}\,\frac{\mu m_H}{k}\,\left(u^2 + \left[\frac{14}{5}\,a_{\mathrm{s}}^2\left(1-\frac{3}{14}\,\frac{a_{\mathrm{s}}^2}{u^2}\right)\right]\right)\,, \tag{2}$$

μ is the mean atomic weight, u is the jump velocity, $a_{\mathrm{s}} = (\frac{5}{3}kT/\mu m_H)^{1/2}$ is the adiabatic upstream sound speed and T the local temperature of the unshocked gas. The term in square brackets is well approximated by $\frac{11}{5}a_{\mathrm{s}}^2$. Note that by inserting u in Eq. (2) instead of the pre-shock velocity we have assumed that the shock is adiabatic with regard to the post-shock temperature but isothermal with regard to the post-shock velocity. This is a consequence of the small cooling length in stellar wind shocks (see Castor 1987).

In the following we will assume that the shock emission is mostly characterized by the immediate post shock temperature T_s of Eq. (2). This neglects the fact that shocks have a cooling structure with a range of temperatures. Then the determination of T_s is equivalent to the determination of the jump velocity u. For our simple and ad hoc approach we adopt

$$u(r)/u_\infty = [v(r)/v_\infty]^\gamma \,, \tag{3}$$

which means that u is correlated with the wind outflow velocity. Furthermore, as a working hypothesis we will assume that u_∞ is proportional to the turbulent velocity $v_{\rm turb}$ which can be determined from the fit of the shape of the P-Cygni profiles (Hamann 1980; Groenewegen et al. 1989). As the simplest approach we assume $u_\infty = v_{\rm turb}$ in Sect. 3. The exponent γ will then be determined empirically.

From Eq. (2) it is evident that $T_s > T$ can only occur for $u > a_s$. With $u_{\min} = m a_s$ we introduce an additional parameter that via Eq. (3) leads to a minimum radius $R_{\min}$ for which the influence of shocks will become apparent. We will use values between $m = 1$ and 4.

Using $\bar{\varepsilon}^s_\nu$ defined in this way the emergent EUV and X-ray spectrum can be calculated from the equation of radiative transfer for a given wind structure. With

$$L_x = \int_{\Delta\nu_x} L_\nu \, d\nu \tag{4}$$

and $\Delta\nu_x$ the frequency range corresponding to the Einstein IPC or ROSAT PSPC, the filling factor f can be adjusted iteratively so that either the observed L_x or a prespecified L_x/L is obtained (an analytical approach for the starting value of f is given in Appendix A).

2.5. Temperature structure

For the calculation of the temperature structure the simultaneous consistent solution of the energy equation (see Fig. 1) is required in principle. However, there are several reasons why the use of a simple approximation is to be perferred at the moment. Because of the complex structure of the NLTE model atoms and the corresponding opacities and emissivities a temperature correction iteration procedure is extremely laborious and time consuming although feasible. Gabler (1992) has extended the "unified model atmosphere approach" of Gabler et al. (1989) and included the bound–bound and bound–free metal opacities of Paper III in the radiative equilibrium as well as the effects of adiabatic cooling. We will use this approach for a few of our models (see Sect. 3 and Fig. 7c).

On the other hand, it is obvious that dissipative processes in the wind (indicated by $H_{\rm diss}$ in Fig. 1) such as shock instabilities and frictional heating [see Springmann & Paudrach 1992 (Paper XI)] will also affect the energy balance. As long as these processes are not taken into account, the wind temperature structure must be regarded as uncertain and its influence on the emergent spectrum has to be investigated using an empirical approach. For this purpose we adopt the simple grey approximation (see for instance Paper I) for the inner regions of the wind. For the outer regions we define ad hoc a wind temperature $T_{\rm wind}$ and adopt $T(r) = T_{\rm wind}$, if the grey approximation temperature falls below $T_{\rm wind}$. Typical values of $T_{\rm wind}$ are 0.6–0.3 $T_{\rm eff}$.

2.6. Hydrodynamics

The algorithm for solving the hydrodynamic equations is described in Papers I, III, IV and VII. The most important step is the calculation of the radiative line acceleration $g^{\rm line}_{\rm rad}$ in the Sobolev approximation at every depth point

$$g^{\rm line}_{\rm rad}(v,r,\rho) = \frac{2\pi}{c\rho}\frac{\pi e^2}{m_e c}\sum_{\rm lines} f_{\rm lu}\left(n_{\rm l} - \frac{g_{\rm l}}{g_{\rm u}}n_{\rm u}\right) \times \int_{\mu_c}^{1} I_c \cdot \frac{1-e^{-\tau_s}}{\tau_s}\mu\,d\mu \,, \tag{5}$$

$g^{\rm line}_{\rm rad}$ is then expressed in terms of the so-called line force multiplier

$$g^{\rm line}_{\rm rad} = \frac{\chi_{\rm Th} L}{c\rho 4\pi r^2} M(t) CF \,,$$

$$M(t) = k t^{-\alpha}\left[\frac{n_e}{10^{11}}\frac{2}{(1-\mu_c)}\right]^\delta ,$$

$$\mathrm{CF} = 2R^2 \int_{\mu_c}^{1} \left[\frac{(1-\mu^2)\frac{v}{r} + \mu^2\frac{dv}{dr}}{\frac{dv}{dr}}\right]^\alpha \mu\,d\mu \tag{6}$$

by a local fit of the force multiplier parameters k, α, δ, which are, as a consequence, depth dependent. $R = r/R_*$, $\chi_{\rm Th}$ is the Thomson opacity and $t = v^{\rm H}_{\rm th}\chi_{\rm Th}/dv/dr$, where $v^{\rm H}_{\rm th}$ is the thermal velocity of hydrogen. CF is the important finite cone angle correction factor (See CAK, Paper I, Friend & Abbott 1986). The solution of the hydrodynamic equations with $g^{\rm line}_{\rm rad}$ given by Eq. (6) then yields the density and velocity structure in the entire sub- and supersonic atmosphere together with the mass-loss rate $\dot{M}$ (see Paper I).

Although depth dependent force multiplier parameters are used for the solution of the equation of motion, the code finally provides mean values for k, α, δ, which yield the same $\dot{M}$ and v_∞ as the converged wind model. These mean values can then be used to calculate the hydrodynamic structure of many wind models with stellar parameters not too different from the original, for spectral analysis or distance determination for instance (see Kudritzki et al. 1992 (Paper X)). However, one has to be careful since it is not always possible to ignore the depth dependence of k, α, δ, as was shown for instance by Pauldrach and Puls (1990, Paper VIII) for the case of P-Cygni.

The influence of line overlaps on $g^{\rm line}_{\rm rad}$ can also be included as described in Paper IV as an additional option. For the results presented in the following sections this was not done, simply because the emphasis of this paper lies more towards spectral synthesis than on an ultimate description of the dynamics.

For reasons of completeness we note that for the contribution of the continuous opacity to the radiative acceleration only Thomson scattering is considered at the moment and free–free and bound–free absorption is neglected. This might be an additional source of uncertainty for models with high mass-loss rates close to the Eddington-limit.

As for the NLTE calculation of the occupation numbers (see Sect. 2.3), the approximate treatment of the EUV line blocking introduces the largest uncertainties for the hydrodynamics. Numerical experiments with either model input fluxes from Kurucz (1979), the new version of the ATLAS 9-code (Kurucz 1992) and ad hoc selected values of $T_{\rm rad}(\nu)$ showed that the mass-loss rate $\dot{M}$ suffers an uncertainty of roughly 30%. Until we can treat the EUV line blocking fully consistently, which will be possible in the forthcoming year (see Sect. 2.3), we have to live with this uncertainty. For the models presented in the next sections model input fluxes from Kurucz (1979) have been used for the calculation of $g_{\rm rad}^{\rm line}$, if not stated otherwise.

2.7. Formal integral

In order to calculate the emergent spectrum, one has to integrate the equation of radiative transfer in the observer's frame with sufficient frequency resolution. Compared to the "formal integral" in static atmospheres, two important additional problems following directly from the velocity induced Doppler-shifts of the lines have to be treated, the formation of lines in narrow resonance zones and the overlap of a large number of lines.

In monotonically expanding atmospheres a single spectral line is formed exclusively in its appropriate resonance zone depending on the observer's frame frequency, the velocity field and the angle between the direction of the ray and the velocity vector. As these resonance zones have a width in velocity space of only a few Doppler widths, they are extremely small in radial extent. As a consequence, a radial "micro-grid" is required in order to perform the integration correctly. For non-over-lapping lines pure Doppler-broadening and negligible continuum opacity this problem can be solved analytically by a linear expansion of the opacity and the source function on the macro-grid. However, in the case of overlapping lines, non-negligible continuum opacity and (in a future version of the code) Stark broadening, a careful numerical integration is needed. For this purpose the method described by Puls & Pauldrach (1990) is used. This is based on a predictor method in order to precalculate the required integration interval so that the resonance zone is sufficiently resolved.

In this way the contribution of overlapping lines at a fixed observer's frame frequency $\nu_{\rm obs}$ can be taken into account correctly. All lines with transition frequencies ν_0 in the range $\nu_0 = \nu_{\rm obs}\,[1 \pm (v_\infty/c)]$ are coupled radiatively (cf. Paper IV and references therein) and have to be considered simultaneously in the line transfer. As an example, the maximum number of overlapping lines in the wavelength range 900–1800 Å that was encountered in the calculations is about 50, a figure that can be treated easily with our algorithm.

As first shown by Hamann (1980), Paper IV and later by Groenewegen et al. (1989) the assumption of a microturbulent velocity $v_{\rm turb}$ is needed to fit the observed UV P-Cygni profiles of strong lines. The physical need to introduce this fit parameter might be explained by the shock instabilities of the wind flow (see Sect. 2.4) and $v_{\rm turb}$ is thought to be related to the shock jump velocities. In consequence, the formal integral can account for microturbulence by adopting a depth dependent $v_{\rm turb}(r)$ of the form

$$v_{\rm turb}(r) = \max\left[v_{\rm turb}^{\rm min},\, v_{\rm turb}^{\rm max}\,\frac{v(r)}{v_\infty}\right].$$

The minimum turbulent velocity $v_{\rm turb}^{\rm min}$ is usually chosen to be of the order of the sound speed ($v_{\rm turb}^{\rm min} = 2a_{\rm s}$ is a good empirical value for the lower wind), the maximum value $v_{\rm turb}^{\rm max}$ can be determined from the shape of strong saturated lines (see Groenewegen et al. 1989).

In the line transfer the continuum background opacity is taken into account consistently. Rotational broadening, which is important for weak lines formed in the region around the sonic point, can be performed as an additional option.

3. Spectrum synthesis and a detailed comparison with observations

We apply our improved code to two objects, the galactic O4f-star ζ Puppis and the LMC O3f-star Melnick 42. ζ Puppis is well observed, since excellent high resolution UV spectra including the important FUV spectral range have already been obtained with the Copernicus satellite (Morten & Underhill 1977). In addition, the effects of free–free emission of the stellar wind on the energy distribution at longer wavelength can also be used to constrain the models, since accurate flux measurements at radio-, mm-, sub-mm- and IR-wavelengths are available.

Melnick 42 has been observed recently with the Hubble Space Telescope (Heap et al. 1991). It is a very luminous object located, at a well known distance, in the 30 Doradus complex of the LMC. The analysis of the high resolution UV spectrum carried out by Heap et al. (with four of us at coauthors) led to an uncertain result with regard to the mass-loss rate. While the fit of the stronger wind metal lines resulted in a low value of $\dot{M}$, the He II 1640 indicated a much higher $\dot{M}$ in agreement with the stellar emission of Hα and He II 4686 in the optical spectrum (see Sellmaier et al. 1993). Walborn et al. 1993 noted that Mk 42 is of the spectral type O3If*/WN6-A and suspected that the presence of an incipient WN envelope might affect the hydrogen and helium lines and that, therefore, conventional O-type models might be insufficient.

This is a very interesting aspect. The analyses of the "photospheric" hydrogen and helium lines by means of hydrostatic NLTE model atmospheres yielded almost identical $T_{\rm eff}$ and $\log g$ for ζ Puppis and Mk 42. However, the UV spectra look rather different. In the present paper we will investigate whether a higher $T_{\rm eff}$ for Mk 42 can provide a solution, satisfying the observational constraints.

3.1. *Analysis of the wind spectrum of ζ Puppis*

The effective temperature of ζ Puppis has been determined from the ionization equilibrium of optical He I and He II absorption lines using excellent spectra of high signal to noise ratio (Kudritzki et al. 1983; Bohannan et al. 1986; Voels et al. 1989). We adopt a value of $T_{\rm eff} = 42\,000$ K. With this temperature and the known distance a radius between 16 and $20 R_\odot$ was obtained. We adopt $R_* = 19 R_\odot$ which then gives $\log L/L_\odot = 6.006$.

For the gravity a value of $\log g = 3.5$ was derived from the fit of Hγ. However, since the NLTE analyses were based on hydrostatic models that neglect the important effect of contamination of the photospheric Hγ absorption profile by stellar wind emission (see Gabler et al. 1989; Sellmaier et al. 1993) we suspect this value to be too low. We will determine this parameter from the observed value of v_∞.

3.1.1. Wind dynamics

The observed value of the terminal velocity is $v_\infty = 2260\,{\rm km\,s^{-1}}$ (Groenewegen et al. 1989; Paper X). A sequence of models with varying $\log g$, but the adopted values of $T_{\rm eff}$ and R_* yielded $\log g = 3.625$ to fit v_∞. The difference of ≈ 0.1 dex with the value obtained from the Hγ NLTE analysis neglecting wind effects is exactly the value obtained by Sellmaier et al. (1993) from their Hγ calculations including winds. Consequently we adopt $\log g = 3.625$ for the gravity of ζ Puppis which gives $M/M_\odot = 55.6$.

With these parameters and the abundances of Sect. 3.1.4 we obtain a mass-loss rate of

$$\dot{M} = 5.1\ 10^{-6} M_\odot\ {\rm yr}^{-1}\,,$$

corresponding to depth independent force multiplier parameters of

$$k = 0.085, \qquad \alpha = 0.657, \qquad \delta = 0.095\,.$$

We note that this value of $\dot{M}$ is significantly larger than calculated previously (Papers IX and X). This is mostly caused by the change in the iron opacity due to the more accurate and complete atomic data (see Sect. 2.1). In Sect. 3.1.5 ii, we will discuss whether this value is in agreement with the observed radio flux and the Hα data.

For the following investigation the hydrodynamic structure of this model will be used. The different assumptions for the subsequent NLTE spectrum synthesis calculations are summarized in Table 2.

3.1.2. Influence of EUV line blocking:
constraints on the wind temperature

For the first spectrum synthesis calculation (model 1 in Table 2) we adopt the simple assumptions of Papers VII and

Table 2. The wind models of ζ Pup

model	T_e	blocking	shocks	$\log L_x/L_{\rm bol}$	v_t/v_∞	γ	m	$Z/Z_\odot$ He	C	N	O	rest	$\dot{M}$ $(10^{-6} M_\odot$ /yr)
1	$T_e = T_{\rm eff}$	Kurucz	no					1.	1.	1.	1.	1.	5.1
2	NLTE	hydrostatic (N)LTE	no					1.	1.	1.	1.	1.	5.1
3	NLTE	hydrostatic (N)LTE	yes	−6.85	.118	1.	1.	1.	1.	1.	1.	1.	5.1
4	NLTE	hydrostatic (N)LTE	yes	−6.85	.118	0.4	1.	1.	1.	1.	1.	1.	5.1
5	NLTE	hydrostatic (N)LTE	yes	−6.85	.118	0.4	1.	1.63	0.03	15.0	0.2	1.	5.1
6	NLTE	hydrostatic (N)LTE	yes	−6.85	.118	0.4	1.	1.2	0.35	8.0	0.75	1.	5.1
6a	grey	hydrostatic (N)LTE	yes	−6.85	.118	0.4	1.	1.2	0.35	8.0	0.75	1.	5.1
7	NLTE	hydrostatic (N)LTE	yes	−6.85	.118	0.4	1.	1.2	0.35	8.0	0.75	1.	3.1
8	NLTE	hydrostatic (N)LTE	yes	−6.85	.118	0.4	1.	1.2	0.35	8.0	0.75	1.	6.3

1994A&A...283..525P

IX: The wind temperature is fixed at $T(r) = T_{\rm eff}$, solar abundances are assumed and the EUV line blocking shortward of the He II edge is simulated by using the model fluxes calculated by Kurucz (1979) as incident radiation field at the inner boundary. Figure 6a compares the Copernicus (900–1500 Å) and IUE (1500–1800 Å) (Walborn et al. 1985) high resolution spectra with the obtained synthetic spectra.

This comparison is striking in a negative sense. Only the N V resonance line is well reproduced by the calculations. For the rest of the spectrum the fit of the Fe V lines between 1420 and 1480 Å is reasonable. However, the calculated highly excited Fe V lines between 1280 and 1330 Å are too strong. The C IV resonance line is slightly too strong, as well as S VI. The O VI resonance line, although at least produced by these "cool wind" NLTE calculations, is too weak, whereas the excited O V line comes out much too strong in the computations. He II 1640 disagrees completely.

The most striking discrepancy concerns the low ionization stages C III, N III, Si IV and their resonance lines (λ977, 991.6, 1393.8) and excited lines (C III at 1175.7 Å and N III at 1750 Å). While the observations indicate the existence of these ionization stages far out in the wind up to velocity shifts of the order of v_∞, the models predict only photospheric components.

In the following part of this section we concentrate on these low ionization stages. Since their groundstate ionization edges are located just longward of the He II edge (Si IV:

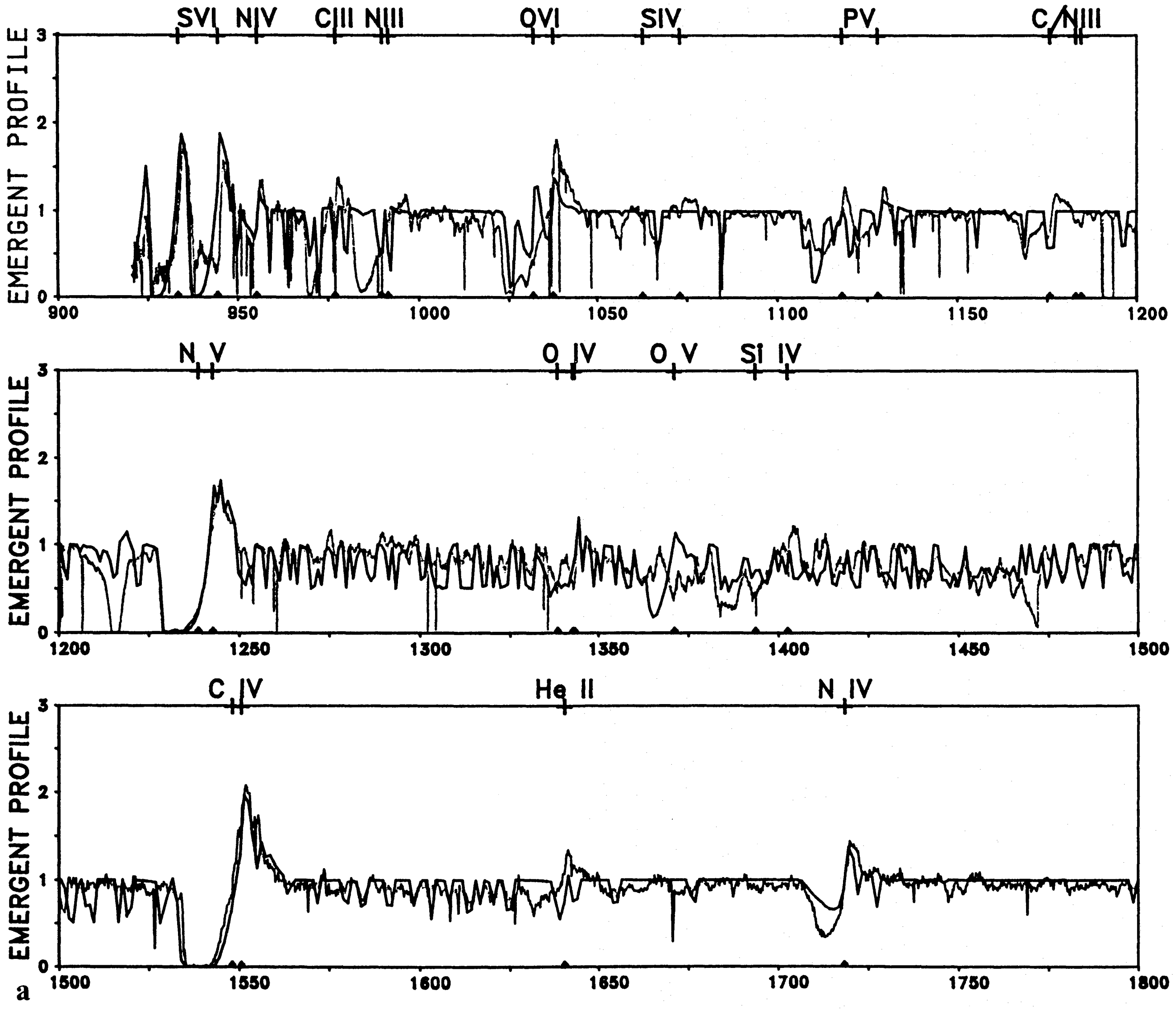

Fig. 6a. Calculated and observed UV spectrum for ζ-Pup. The calculated spectrum belongs to model 1, where shock radiation has been neglected. Kurucz fluxes are used, and the wind temperature has been fixed at the effective temperature. The observed spectrum shows the Copernicus high resolution observation (900–1500 Å, Morten & Underhill 1977) and an IUE high resolution observation (1500–1800 Å, see Walborn et al. 1985)

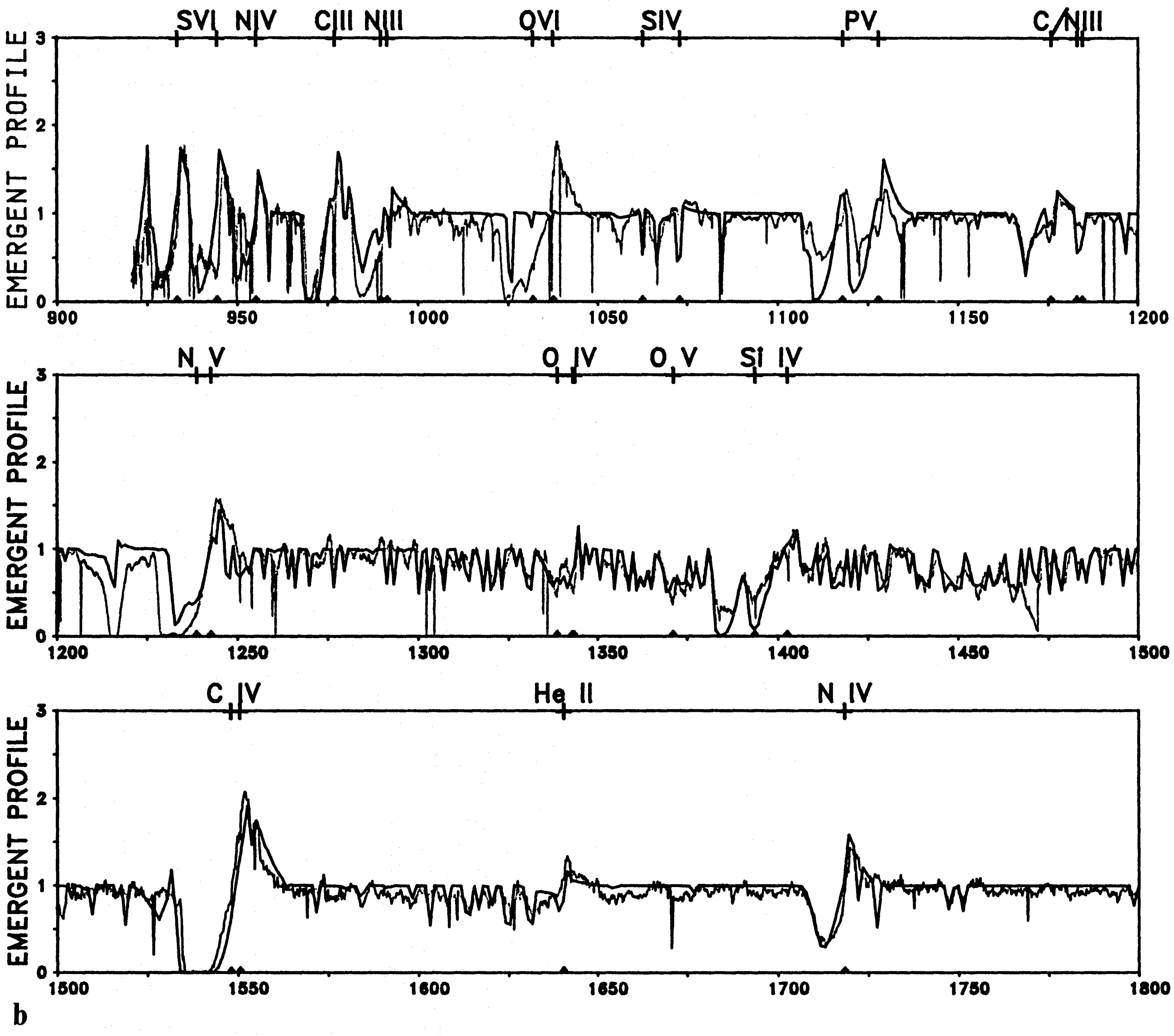

Fig. 6b. Same as Fig. 6a, but for model 2, where shock radiation has been neglected, but line blocked fluxes and a NLTE temperature structure have been considered

274.4 Å: N III: 261.4 Å; C III: 258.9 Å), where the continuum opacity is small and optical depth unity is reached deep in the photosphere, it is obvious that the discrepancy can be attributed to unsufficient line blocking in the radiative ionization rates calculated from the old Kurucz fluxes of 1979 (see Sect. 2.3). Test calculations of photospheric models with more detailed opacities (see Sect. 2.3, Fig. 3) confirm this suspicion and indicate that a photospheric radiation field corresponding to $T_{\rm rad} = 31\,000$ K is more appropriate between 227 and 300 Å (see Fig. 6d).

Using such a photospheric radiation field as input to the wind NLTE calculations we achieve only partial improvement for the low ionization stages. We still fail to reproduce the resonance lines at wavelengths corresponding to high velocity shifts or, in other words, far out in the wind the population of these stages is still too low. The reason for this behaviour lies in the fact that the ground state ionization edges are very close to that of He II (227 Å). In the outer wind layers of model 1 the continuum shortward of the He II-edge becomes optically thin and the corresponding radiation field starts to contribute significantly to the ionization of C III, N III, Si IV so that these stages almost disappear.

The only way to avoid this situation is by recombination of He III to He II in the outer wind layer. In this case the opacity shortward of 227 Å is strongly enhanced, the radiation field is reduced due to the optical thickness and the ionization is restricted. In addition, recombination of helium would also explain why the He II subordinate line λ1640 is observed up to very high outflow velocities.

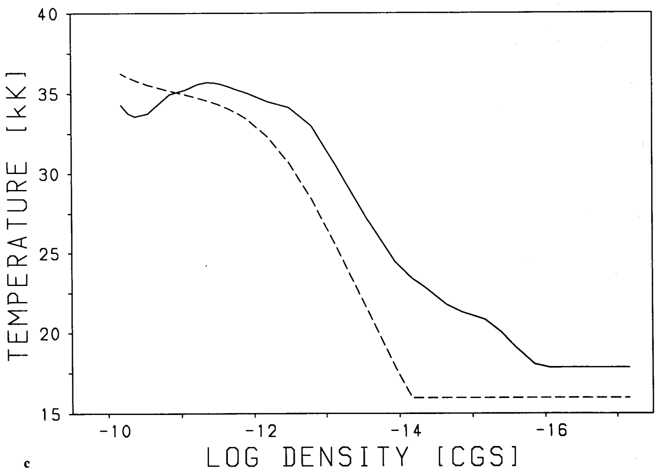

Fig. 6c. Temperature versus density in the wind part of ζ-Pup. The fully drawn curve represents a spherical NLTE-model which includes metal opacities, while the dashed curve corresponds to a spherical grey model

Gabler et al. (1989, see their Appendix) have shown that the helium ionization depends on the local kinetic temperature of the wind and the radiation temperature of the incident photospheric radiation field at the wavelength of the He II resonance line (304 Å). Lowering both values will strongly reduce the helium ionization. The line blocking simulations (see Sect. 2.3) indicate that $T_{\rm rad} = 39\,000$ K is a reasonable value between 300 and 375 Å. Moreover, the stellar wind radiative equilibrium calculations by Gabler (1992) yield a significant drop in the kinetic temperature below 0.6 $T_{\rm eff}$ (see Fig. 6c and Sect. 2.5). A test calculation with this $T_{\rm rad}$ and temperature structure proved indeed that helium recombined and the ionization stages of C III, N III, Si IV were enhanced in the outer wind layers.

The radiation field below the hydrogen Lyman edge is not only responsible for the ionization of the lower stages but also for the excitation of the lower levels of the excited lines of O V at 1371 Å and N IV at 1718 Å. The wavelengths of the exciting transitions are at 629.7 and 765.1 Å, respectively. As indicated by Fig. 3 line blocking is also impor-

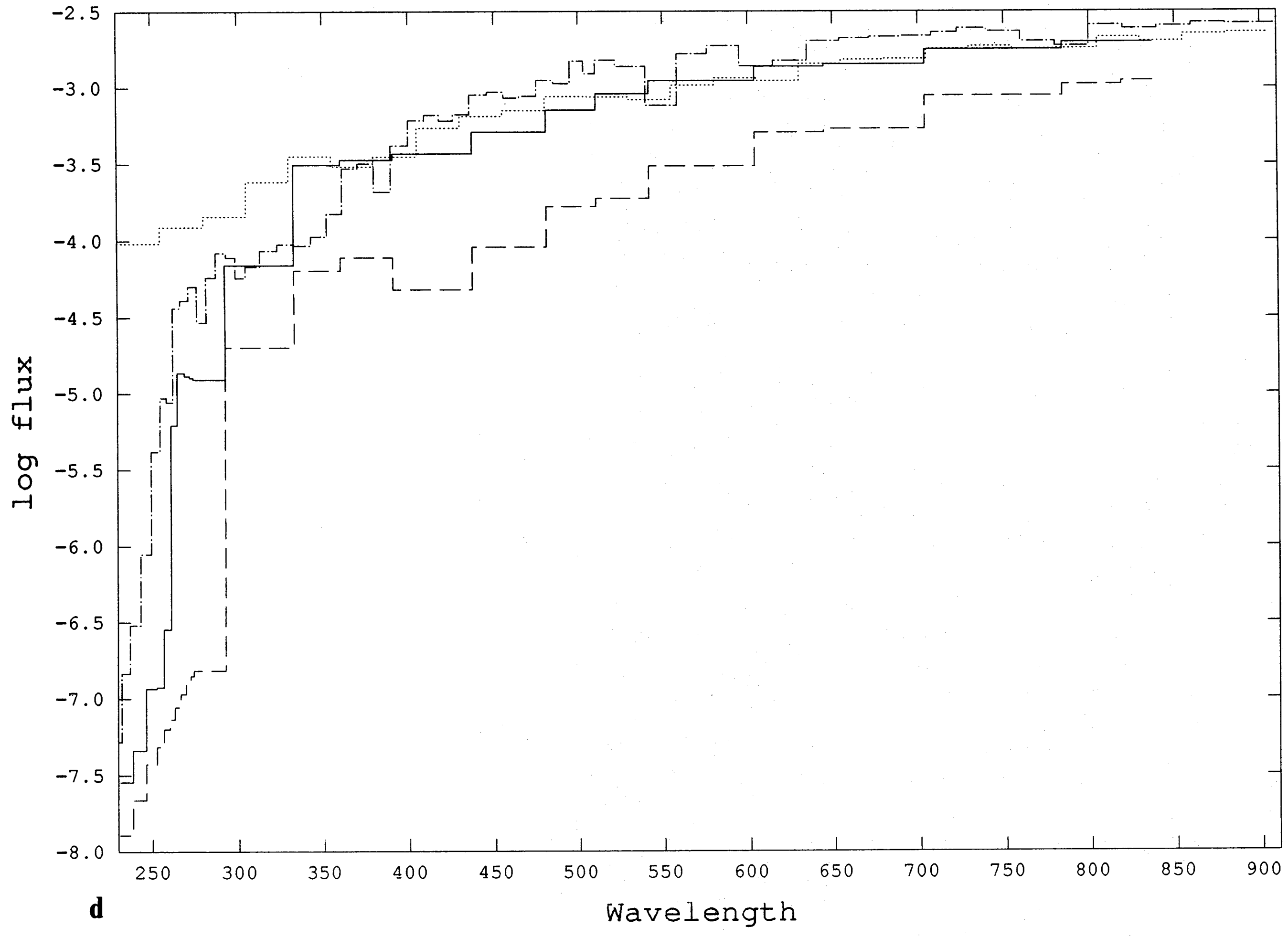

Fig. 6d. Logarithm of the smoothed mean structure of the emergent flux (erg cm^{-2} s Hz^{-1}) of photospheric models of ζ-Pup in the range 227–911 Å. The fluxes are from Kurucz (1979) – dotted, the ATLAS 9-code – dash-dotted, hydrostatic (N)LTE (Fig. 3) – fully drawn, and our procedure – dashed

tant at these wavelengths. Thus, we have adopted a value of $T_{\rm rad} = 34\,000$ K from 375 to 911 Å. (Note that according to test calculations the influence of line blocking is better described by the lower limit of the emergent flux calculations shown in Fig. 3 than by introducing smoothed average values – see Fig. 6d. This is not surprising, as the photospheric blocking shown in Figs. 3 and 6 is based on LTE line formation calculations).

Figure 6b shows the synthetic spectrum of model 2 calculated with $T(r)$ according to Gabler (1992, see Fig. 6c) and $T_{\rm rad}(\lambda)$ split into three domains between 227 and 911 Å as described above. Regarding C III, N III and Si IV the situation has clearly improved although Si IV now appears to be too strong. He II 1640 also shows a high velocity component in the theoretical spectrum, the profiles of N IV and O V are matched perfectly and the Fe V lines are represented well.

On the other hand, these improvements for the lower and intermediate ionization stages are accompanied by increased deficiencies for high ionization. The fit of O VI has become worse and N V, which was perfect before, is now too weak. As we will show below, these deficiencies disappear as soon as the EUV radiation field of shocks is accounted for.

3.1.3. The influence of EUV and soft X-ray shock radiation

The next step is to include the effects of shock emission as described in Sect. 2.4. Following Chlebowski et al. (1989) we adopt $\log(L_X/L_{\rm Bol}) = -6.85$. Groenewegen et al. (1989) have determined a maximum turbulence velocity of $v_{\rm turb} \simeq 0.118 * v_\infty$. We adopt this value for the maximum shock jump velocity u_∞. Then, the only free parameters are the exponent γ, which couples the shock jump velocity with the outflow velocity, and m, which defines the inner boundary for the onset of shocks. As all test calculations have shown, the effect of variations of m between 1 and 4 on the resulting O V spectrum is small. We thus adopt $m = 1$ throughout this section. For γ we start with the simplest case $\gamma = 1$, i.e. a constant ratio between shock and local velocity in the wind (model 3). In a further model (model 4) we allow for an increase of shock velocity and shock temperature inwards by setting $\gamma = 0.4$.

Figure 7 compares the synthetic spectra of models 3 and 4 with the observations and reveals the importance of the direct ionization due to EUV and soft X-ray photons emitted by shocks (the discussion will be postponed to Sect. 3.1.5 iii,). The very simple case $\gamma = 1$ leads to a large improvement in N V and O VI, while $\gamma = 0.4$ improves the fit of O VI significantly. O VI is obviously very sensitive to the shock temperature stratification and the resulting radiation field.

Si IV is also marginally affected by shock emission, at least for $\gamma = 0.4$, as indicated by Fig. 7b. The reason is the soft X-ray radiation field of the shocks, which enhances the ionization of Si V (ionization edge at 74.3 Å) and, therefore, decreases the recombination to Si IV.

3.1.4. Determination of abundances

Up to now solar abundances have been assumed in our calculations. However, the analysis of the photospheric He II Pickering lines ($\lambda\lambda$3293, 4200, 4542) has led to the conclusion that ζ Puppis has an enhanced helium abundance. Kudritzki et al. (1983) determined a helium number fraction of $n_{\rm He}/n_{\rm H} = 0.163$, Voels et al. (1989) obtained 0.25. If this enhancement of helium is caused by mixing with CNO-burned matter, the abundances of carbon and oxygen should be smaller than solar and nitrogen should be strongly enhanced. The fact that the C III resonance line of model 4 is too strong and the N III resonance line is too weak, indicates that this might be true. Both lines are affected in the same way by the photospheric $T_{\rm rad}$ and the temperature structure $T(r)$. Thus relative abundances derived from these two lines should be quite accurate.

Taking predictions from evolutionary tracks for massive stars ($M_{\rm ZAMS} = 60 M_\odot$) with mass-loss and convective mixing (Maeder 1990) we would expect $\varepsilon_{\rm c} = 0.03\varepsilon_{\rm c,\odot}$, $\varepsilon_{\rm N} = 15\varepsilon_{\rm N,\odot}$ and $\varepsilon_{\rm o} = 0.2\varepsilon_{\rm o,\odot}$ for $n_{\rm He}/n_{\rm H} = 0.163$ ($\varepsilon_{x,\odot}$ are the solar number fractions).

We have, therefore, calculated a model 5 with these modified abundances. The synthetic spectrum is shown in Fig. 8. The comparison of the C III/N III resonance lines indicates that this is most probably too large a change in the C/N ratio. The calculated N III line now shows a pronounced P-Cygni profile with too strong emission and absorption. C III is marginally too weak. In addition, N V and N IV are too strong, whereas the excited line C III at 180 Å is also too weak. C IV is problematic. The emission peak is too weak but the absorption trough is too broad. The excited lines of N III at 1750 Å are almost photospheric and do not change within this range of abundance variations. Effects of the oxygen abundances are only marginally seen in the tip of the O VI emission, whereas O V and O IV remain unaffected. He II 1640 does not show any abundance effect at all.

In model 6, for which the synthetic spectrum is shown in Fig. 9, we have adopted $\varepsilon_{\rm c} = 0.35\,\varepsilon_{\rm c,\odot}$, $\varepsilon_{\rm N} = 8\varepsilon_{\rm N,\odot}$, $\varepsilon_{\rm o} = 0.75\,\varepsilon_{\rm o,\odot}$. According to the evolutionary tracks of Maeder (1990) this would correspond to $n_{\rm He}/n_{\rm H} = 0.12$. The calculated carbon lines now show reasonable strength, although the problem with the absorption trough of the C IV resonance line remains (note that compared to the Copernicus observation the emission peak is now almost perfect). N III, IV and V are still moderately too strong. A further reduction of the nitrogen abundance by a factor of two but the same carbon abundance would result in a better fit. However, in view of the uncertainties in our model calculations we regard model 6 as our current best model.

We conclude that our spectrum synthesis technique does, in principle, allow the determination of abundances. We can reproduce the UV Fe V spectrum of ζ Puppis with solar abundances. Carbon and nitrogen show indications of the CNO-process. The profiles of all other lines can be matched by assuming solar abundances apart from the P V line which

1994A&A...283..525P

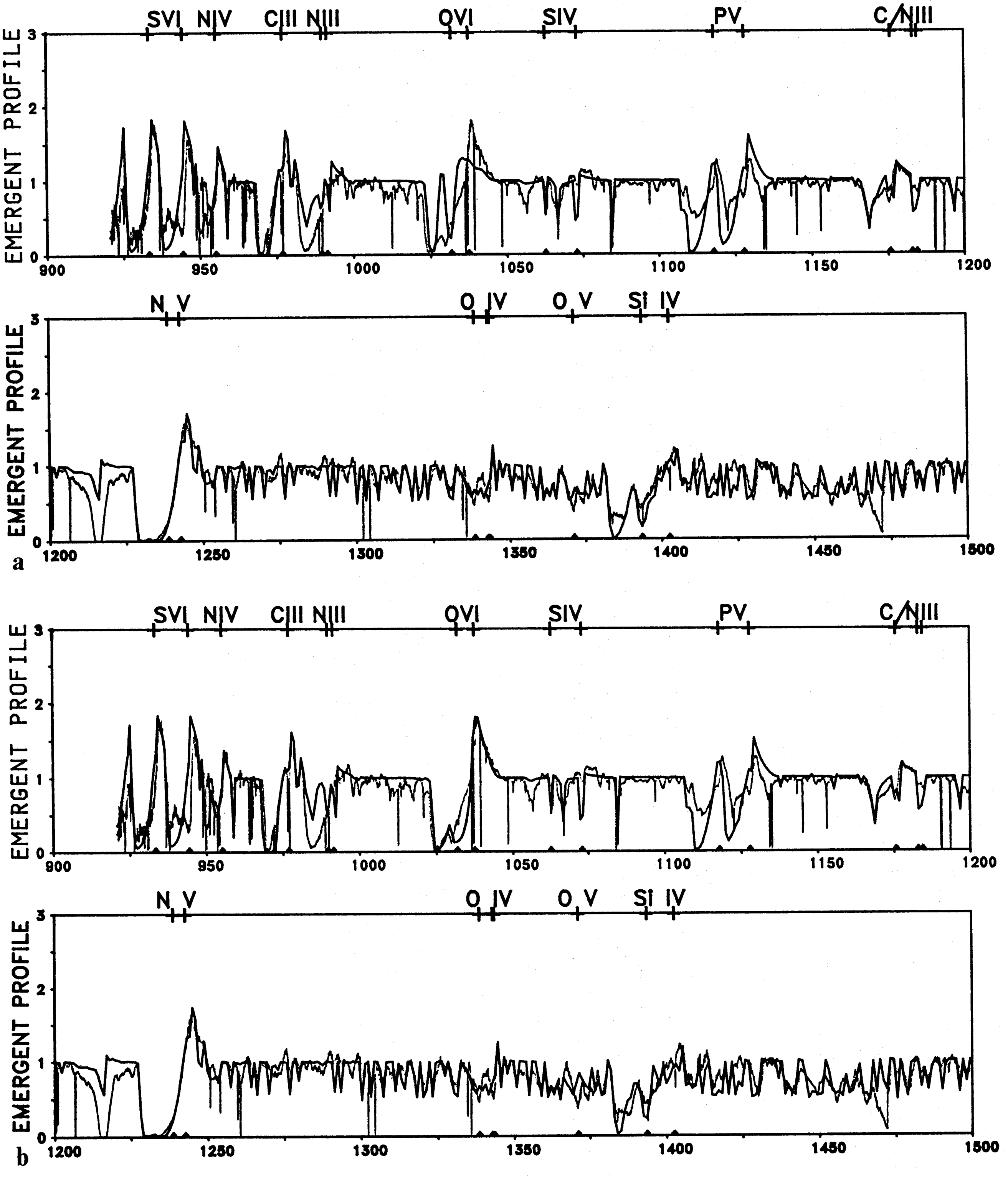

Fig. 7a and b. Same as Fig. 6b, but for models 3 and 4, where shock radiation has been included with two different values of γ. $\gamma = 1.0$ (**a**) and $\gamma = 0.4$ (**b**)

indicates that the P-abundance is a factor of 1.5–2 less than solar.

It is very likely that the discrepancy between the observed and calculated P v resonance line profile is caused by an abundance effect. P v together with P vi are the major ionization stages (P iv is a trace ion). Since the P v groundstate ionization threshold ($\lambda = 191$ Å) is very close to that of He ii, the P v ionization is entirely controlled by

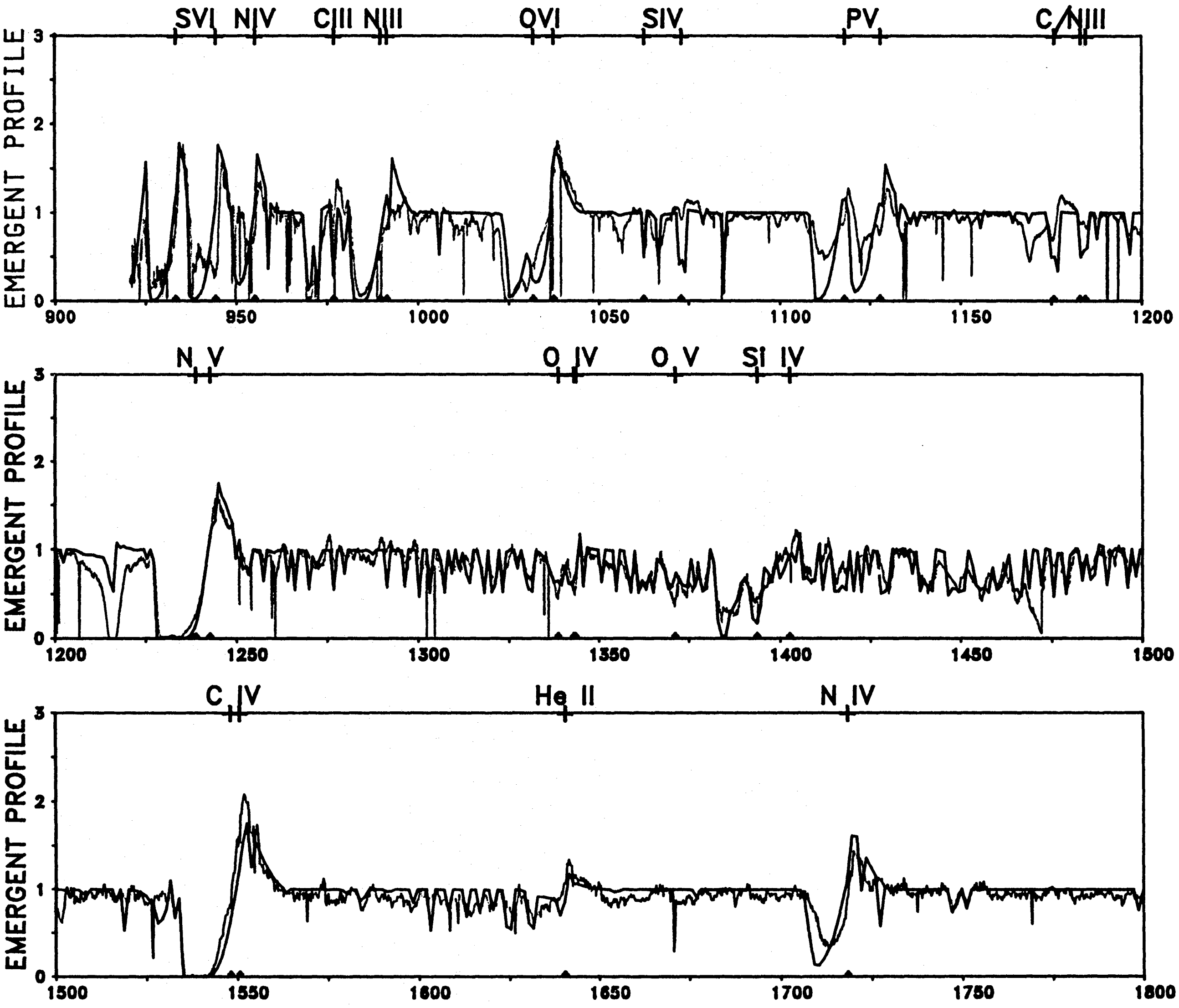

Fig. 8. Same as Fig. 7b, but for model 5, where abundances corresponding to a He number fraction of $N_{\text{He}}/n_{\text{H}} = 0.163$ have been assumed

the He II opacity. On the other hand, P VI is isoelectronic with a rare gas and, therefore, only marginally affected by shock emission so that simple direct recombination to P V is the dominating depopulation process for P VI. Consequently, the ionization fraction of P V should be of a similar accuracy to that of He II. The same argument as for P V holds also for S VI, the next ionization stage in the isoelectronic sequence. Here, the agreement between the calculated and observed resonance line profiles is satisfactory and, therefore, a solar sulphur abundance appears to be appropriate.

3.1.5. Additional remarks

(i) Influence of the wind temperature stratification. From the results above we deduced that the local kinetic temperature has to decrease below $0.6T_{\text{eff}}$ in the outer part of the wind in order to describe the low ionisation stages correctly. Since the computational effort to calculate an accurate NLTE temperature structure in radiative equilibrium including metal line opacity and adiabatic expansion is formidable (see Gabler 1992), we have also investigated as to whether a detailed accurate temperature structure is really required. For this purpose we recalculated model 6 using a spherical grey temperature structure set to a constant when $T(r)$ reaches $0.35T_{\text{eff}}$ in the outer part. The resulting spectrum is shown in Fig. 10. Even a thorough comparison of Figs. 9 and 10 does not reveal significant differences. We thus conclude that the spectral features in the UV do not depend crucially on the local wind temperature stratification as long as the temperature is reasonable in the inner subsonic part and decreases below a certain level in the outer part, so that helium can recombine.

(ii) Discussion of the mass-loss rate. Model 6 as our preferred model yields a mass-loss rate of $\dot{M} = 5.1\ 10^{-6} M_{\odot}$ yr^{-1} as a result of the self-consistent hydrodynamic

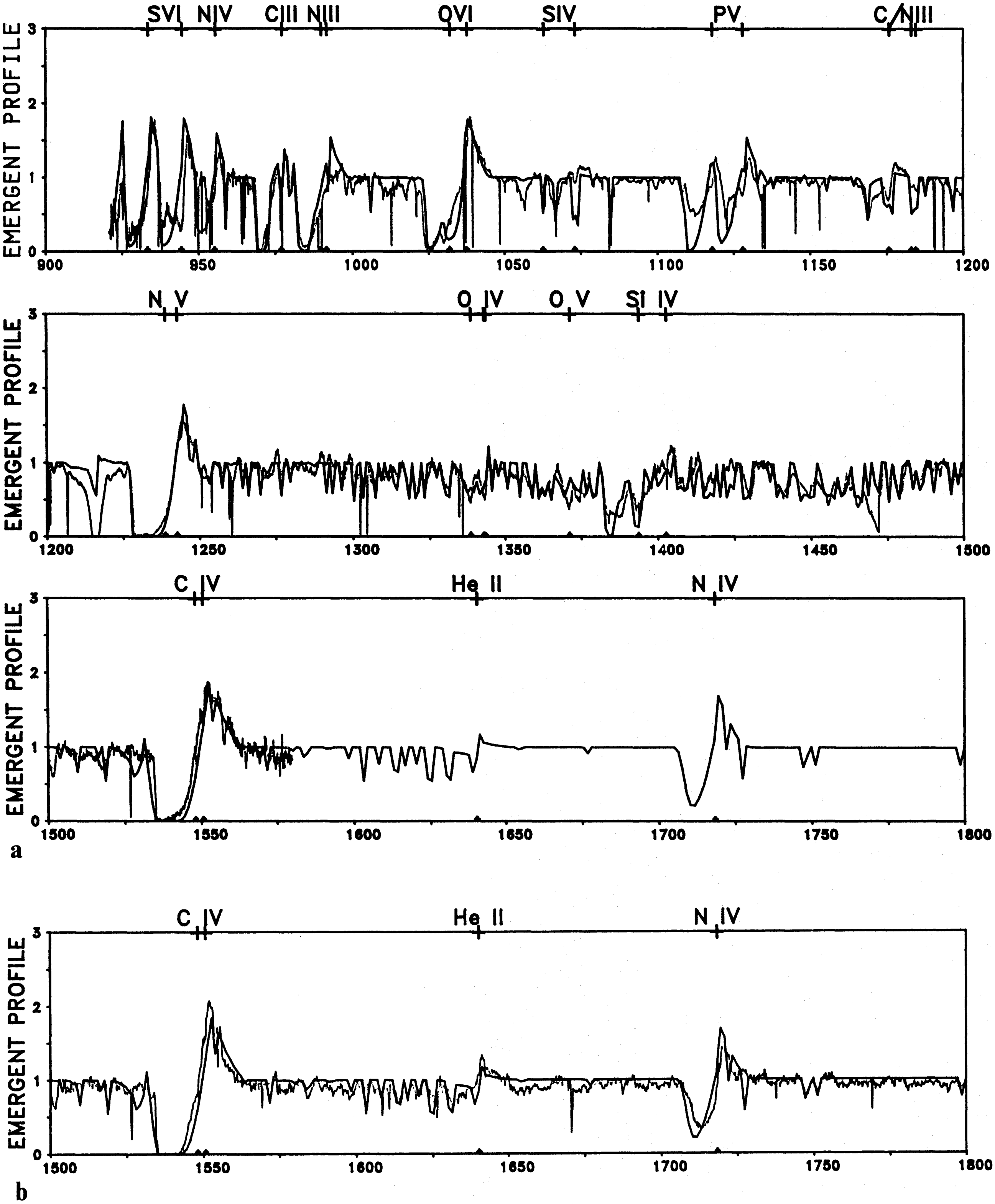

Fig. 9a–c. Same as Fig. 7b, but for model 6 – our current best model, where abundances have been determined using our procedure. **a** shows the comparison with the Copernicus spectrum, **b** with the IUE spectrum and **c** shows the C III and N III resonance lines on a larger scale

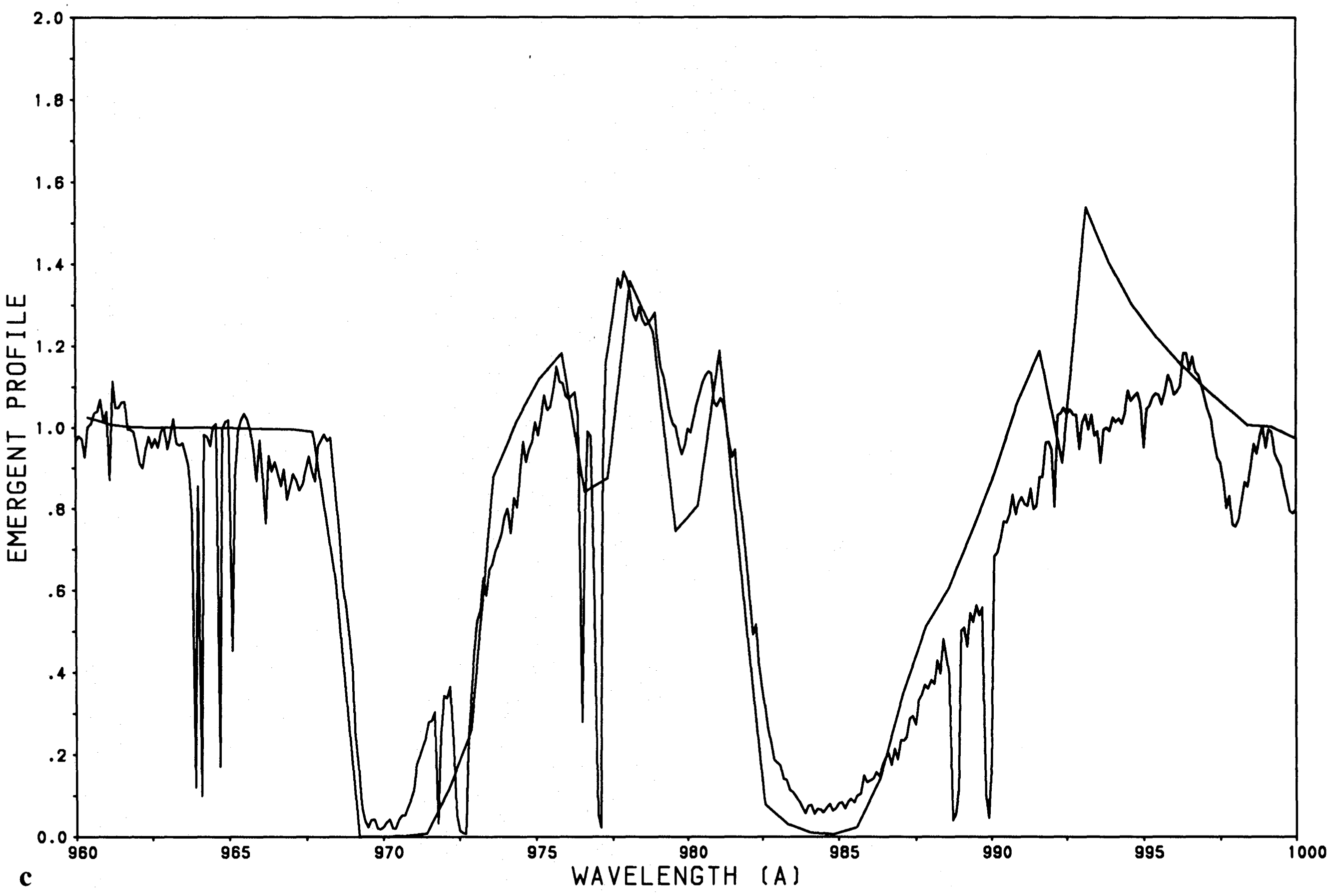

Fig. 9 (continued)

calculations. Following the discussion in Sect. 2.6 we regard this theoretical value as uncertain to within ± 30%.

The observed radio flux [3.0 10^{-3} Jy at 2 cm (Abbott 1985) and 1.4 10^{-3} Jy at 6.4 cm (Abbott et al. 1980)] together with a distance of 450 pc (corresponding to $R = 19 R_\odot$) and the observed value of v_∞ allows an estimate of the mass-loss rate to be made using the formula by Wright & Barlow (1975) for cool wind bound–free and free–free emission. Taking into account the $\mathrm{He}^{++} \rightarrow \mathrm{He}^{+}$ recombination and a cool wind temperature of $T = 0.4\,T_{\rm eff}$ we obtain $\dot{M}_{\rm radio} = 3.9^{+1.0}_{-0.8}\ 10^{-6} M_\odot\ {\rm yr}^{-1}$.

This can be regarded as agreement between theory and observation within the present uncertainties.

To investigate whether the UV spectrum synthesis allows us to discriminate between models in the ± 30% range of $\dot{M}$ we have calculated the models 7 and 8 for $\dot{M} = 3.1$ and 6.3 $10^{-6} M_\odot\ {\rm yr}^{-1}$, respectively (Fig. 11). The differences are small but significant. Model 7 gives a better fit to N IV and perhaps Si IV, whereas model 8 reproduces He II 1640 and C III 1180 somewhat better. This does not allow a final conclusion on $\dot{M}$ to be made from the viewpoint of UV spectrum synthesis.

(iii) Energy distribution. To demonstrate the effects of shocks Fig. 12 shows the energy distribution calculated for models 2 and 6 (note that metal line blocking between 228 and 911 Å was not taken into account in this particular energy distribution calculation, since effects are seen only shortward of 228 Å and at infrared/radio wavelengths). The influence of shock emission shortward of the He II edge is significant. Since the local mean intensity $J_\nu(r)$ is more important than the emergent flux for the ionization calculation within the wind, we give the ratios of shock to cool wind emission coefficients and the related mean intensities as functions of radius and wavelength in Table 3. Note that at these wavelength the radiation field is optically thick up to the largest radius in Table 3. The enormous importance of the shock emission for the direct ionization is evident. Moreover, since the ratio of $J_\nu^{\rm tot}/J_\nu^{\rm sw}$ changes by just 2 dex from 1.65 to $76 R_*$ at the C IV edge, while a change of almost 12 dex occurs at the O VI edge, we conclude that the influence of shock radiation starts at smaller radii with lower shock temperatures at longer wavelengths, whereas for shorter wavelengths the largest shock temperatures dominate. Thus, the X-ray spectral region will be affected by the terminal shock temperature (see also

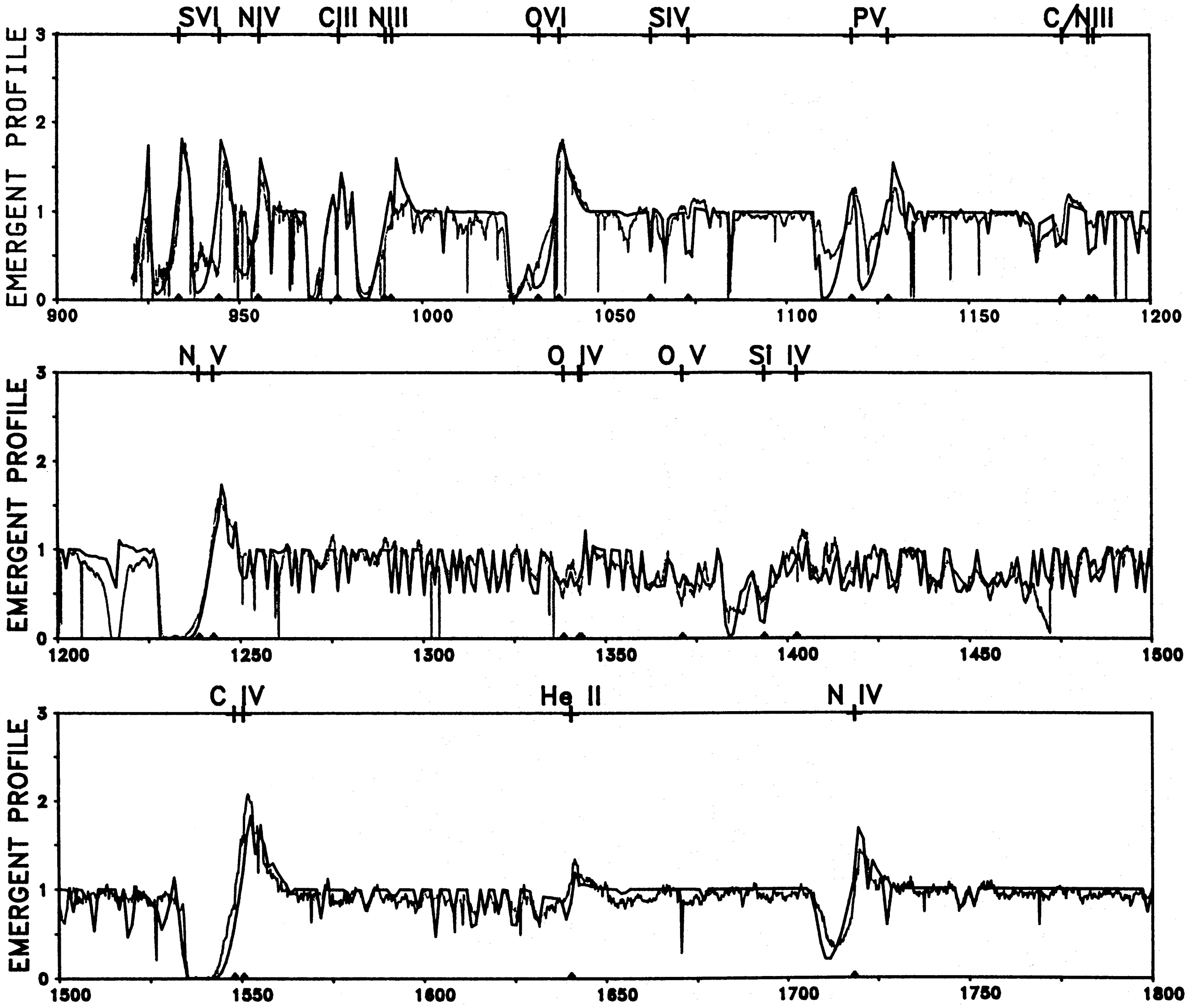

Fig. 10. Shows the comparison of the best model (6) calculated with a spherical grey temperature structure

Hillier et al. 1993), whereas the EUV part provides constraints on the lower shock temperatures.

Surprisingly, the shock emission has a non-negligible influence at radio (10%) and IR (30%) wavelengths, as Fig. 12 indicates (note that the approximation given by Abbott et al. (1986) was used for the free–free Gaunt factor in the radio part). This conclusion is, of course, based on our simplifying assumption of a wavelength independent ratio between the free–free and line emission of the hot shocked plasma. Existing coronal codes do not allow us to investigate whether this assumption is still reliable at these long wavelengths or whether it breaks down completely. Further investigation will be needed.

As a first test we have compared 'the predicted fluxes of models 2 and 6 with the ζ Puppis IRAS observations (Lamers et al. 1984) in Table 4. Tentatively we conclude that shock emission might be observable in the IR. For the forthcoming ISO mission this might become very important. (We note that this effect would be strongest in the case of smaller mass loss rates where the radio continuum becomes optically thin at less than 50 stellar radii and thus the radio spectral region can be influenced strongly by shock emission. This influence could easily explain the discrepancies that exist between predicted and observed radio mass loss rates and between observed and predicted IR-fluxes for some O-stars – e.g. the 09.5 Ia-supergiant α-Cam – see Paper IX).

Figure 12 requires an additional comment. It does not show the enhancement of the EUV flux shortward of the He II-edge as found by Gabler et al. (1989). This is caused by the low value of T_e in the outermost part of the wind which causes the He II continuum to be optically thick up to more than $100R_*$ and thus reduces the flux shortward of the He II-edge significantly. Since this behaviour is enhanced by the EUV line

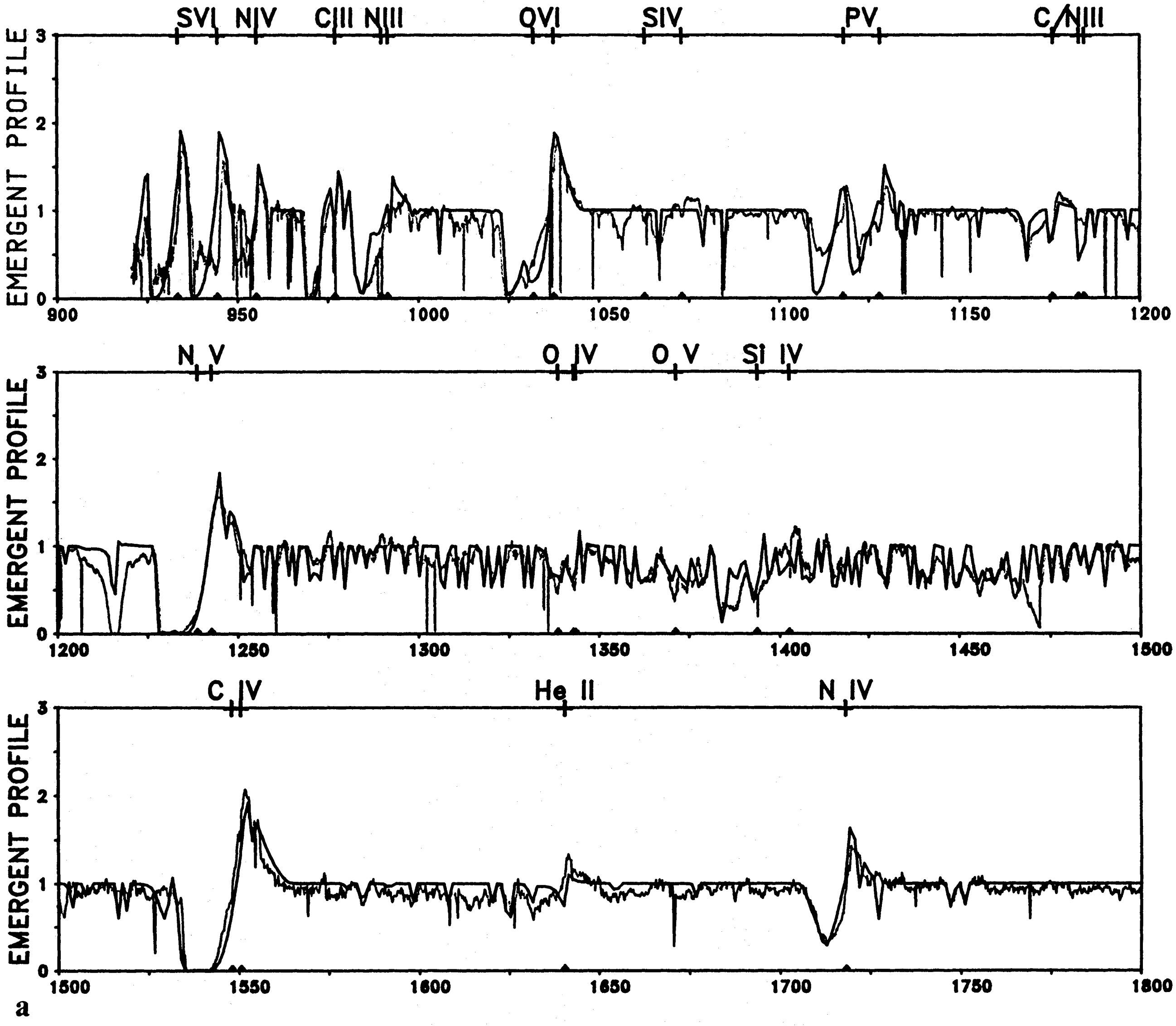

Fig. 11a and b. Same as Fig. 9, but for models 7 and 8, wehre a smaller (**a**) and a larger (**b**) mass loss rate have been assumed, respectively

blocking which yields a lower $T_{\rm rad}(\nu)$ at the wavelength of the He II resonance line (see Sect. 3.1.2), we believe that this is a more realistic description for O-stars around $T_{\rm eff} = 40\,000$ K such as ζ Puppis as also confirmed recently by observations of emission line fluxes of the nebula surrounding Θ^1 C Ori (Pakull 1992). On the other hand, for much hotter objects like Central stars of Planetary Nebulae or metal poor very hot O-stars in Giant Extragalactic H II regions, the effects discussed by Gabler et al. (1991, 1992) might still be important.

(iv) Ionization fractions. For detailed line profile fits and for the calculation of opacities, for instance in the X-ray spectral domain it is important to have the predicted ionization fractions as a function of radius, velocity and density. This information is given in Table 5 for the most important elements.

3.2. Analysis of the wind spectrum of Melnick 42

The UV spectrum of the O3f star Melnick 42 was obtained with the Goddard High Resolution spectrograph on board the HST. Heap et al. (1991) published a first analysis of this spectrum based on stellar parameters obtained by a NLTE analysis of the optical hydrogen and helium absorption lines using hydrostatic NLTE models which yielded

$$T_{\rm eff} = 42\,500 \pm 2000\,{\rm K}\,, \qquad \log g = 3.5 \pm 0.15,$$

$$R_* = 28 R_\odot\,, \qquad n_{\rm He}/n_{\rm H} = 0.10\text{–}0.15\,.$$

The UV analysis carried out using our old stellar wind code

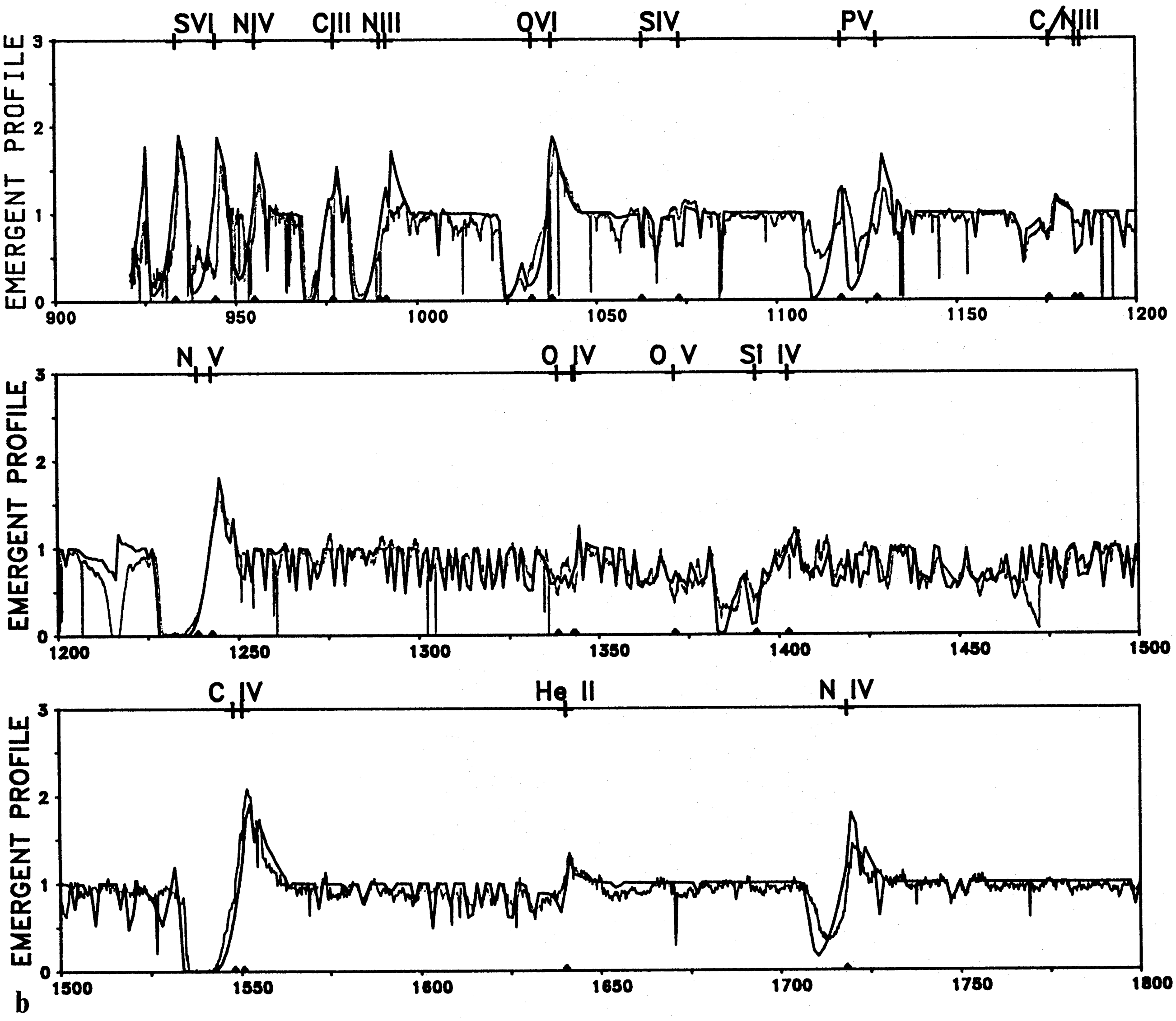

Fig. 11 (continued)

led to the conclusion that the metal abundances of Melnick 42 are roughly reduced by a factor of four except for nitrogen and carbon which appeared to be solar and 1/2 solar respectively. With these abundances and stellar parameters a v_∞ of 3000 km s^{-1} was obtained from the self-consistent radiation hydrodynamics in agreement with the observations and a mass-loss rate of $\dot{M} = 4\ 10^{-6} M_\odot\ \mathrm{yr}^{-1}$, which gave a reasonable fit to the iron spectrum and the stronger stellar wind metal lines, but yielded a poor fit to He II 1640. This line together with Hα and He II 4686 in the optical spectrum indicates a much higher rate of mass-loss (see Sellmaier et al. 1993).

3.2.1. Model at $T_{\mathrm{eff}} = 42\,500$ K

In a first step we investigate whether our new stellar wind code can reduce the discrepancy. For this purpose we use the same hydrodynamic model as Heap et al. (1991) but perform new line formation calculations incorporating all the improvements described in Sects. 2 and 3.1. In particular, we adopt the same values of T_{rad} as for ζ Puppis to simulate the line blocking and we need to specify L_x/L_{Bol}, v_{turb} (= u_∞, the maximum jump velocity) and the stratification exponent γ.

As a result of the line fit procedure of C IV and N V carried out by Heap et al. (1991) $v_{\mathrm{turb}} = 135$ km s^{-1} $= 0.045 v_\infty$ was obtained (Haser, private communication). With Eqs. (2) and (3) this leads to much smaller shock temperatures ($T_{\mathrm{s}} \leq 300\,000$ K) than obtained for ζ Puppis. For γ we adopt = 1.0. Since the X-ray luminosity of Melnick 42 has not been measured so far (a direct measurement with ROSAT for instance will be difficult because of its distance and the large column density of hydrogen), we have to adopt it as a free parameter. We start with a rather small

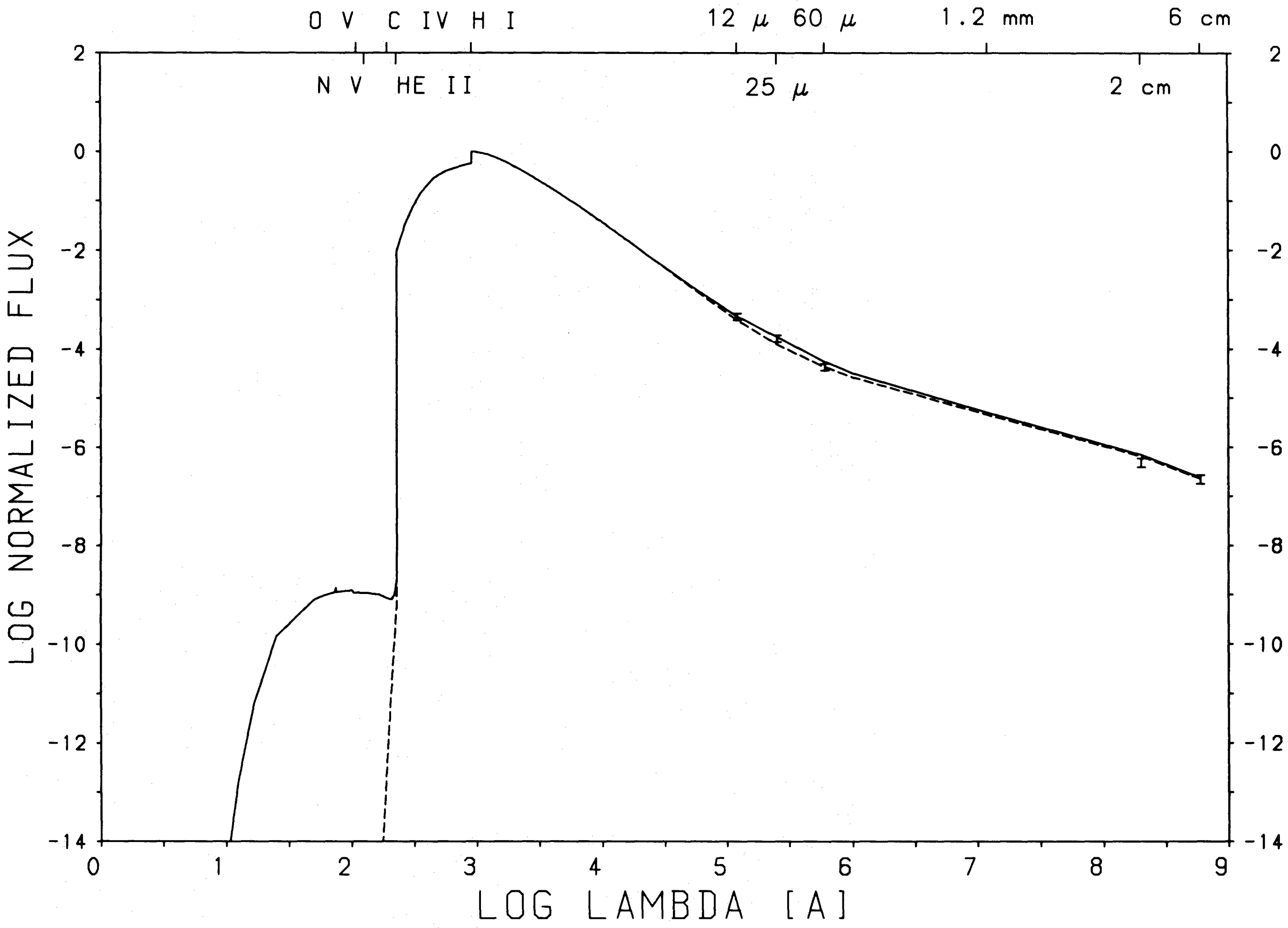

Fig. 12. EUV to radio energy distribution of two atmospheric models – including the shcok emission coefficient (fully drawn) and without (dashed) – of ζ-Pup. The shock emission dominates in the EUV, is negligible in the optical, and influences the infrared and radio spectral regions. The observed radio and infrared data within their error bars are also indicated.

Table 3. The ratios $\log(\varepsilon_\nu^{\rm s}/\varepsilon_\nu^{\rm sw})$ and $[\log(J_\nu^{\rm tot}/J_\nu^{\rm sw})]$ in the optically thick wind of ζ Puppis

No.	R	v/v_∞	T_e/T_{eff}	T_s (10^6 K)	λ(Å)		
					192.2 CIV	108.8 OV	89.8 OVI
1	1.65	.50	.69	.53	- 0.37 [0.18]	0.26 [3.52]	0.80 [6.72]
2	4.3	.83	.54	.89	0.0 [0.36]	0.65 [6.28]	0.84 [10.36]
3	16.6	.96	.45	1.04	0.57 [0.78]	1.90 [9.23]	3.60 [14.11]
4	76.0	.99	.42	1.07	1.45 [2.51]	2.28 [12.15]	4.48 [18.46]

1994A&A...283..525P

value of $\log L_X/L_{\mathrm{Bol}} = -7.3$. (The parameters of all models for Melnick 42 are summarized in Table 6).

In Fig. 13a we compare the calculated spectrum with the observations. Strikingly the new calculations can roughly reproduce the broad desaturated absorption troughs of C IV and N V (note that 1/4 solar abundance was adopted for all metals). This is due to the very strong ionizing EUV radiation field of the low temperature shocks. However, there remain severe discrepancies. He II 1640 is calculated to be in absorption in strong contradiction to the observation O V and N IV are discrepant as well, as is the emission peak of C IV. Moreover, a number of Fe IV absorption lines appear in the calculations between 1580 and 1700 Å which are definitely not present in the observed spectrum (note that these lines did not show up in our older calculations in Heap et al., because of the deficiencies of our old Fe IV model atom).

Table 4. Calculated fluxes for the IR energy distribution of ζ Puppis in units of the observed fluxes

$\lambda(\mu)$	F_ν^{sw}/F_ν^{obs}	F_ν^{s}/F_ν^{obs}
12	0.85	1.03
25	0.76	1.07
60	1.01	1.30

In a next step (model 2) we increase the wind density artificially (corresponding to $\dot{M} = 27\,10^{-6} M_\odot\,\mathrm{yr}^{-1}$) to investigate whether the observed UV spectrum can be explained by a higher mass-loss rate at the same effective temperature. The result is shown in Fig. 13b. The shape of He II 1640 and N IV are now, at least in principle, reproduced correctly. However, the Fe IV lines are now much stronger and severely discrepant. In addition, strong Si IV absorption appears which is not observed. The same is true for C III.

Table 5. Important ionization ratios ($n_{\mathrm{I}}/n_{\mathrm{H}}$) for model 6 of ζ-Pup at selected points in the wind

R	1.005	1.025	1.07	2.00	7.32	13.3	76.0
n_H (cm^3)	2.6(13)	7.8(11)	2.5(11)	1.1(10)	5.5(8)	1.6(8)	4.6(6)
HeII	2.3(−2)	8.1(−5)	9.0(−5)	1.1(−3)	5.0(−2)	9.1(−1)	1.1(−1)
CIII	1.7(−6)	3.4(−9)	2.0(−9)	1.6(−8)	3.1(−7)	8.0(−7)	4.0(−6)
CIV	1.6(−4)	7.1(−6)	8.0(−6)	5.7(−5)	1.6(−4)	1.6(−4)	1.6(−4)
NIII	2.5(−5)	4.0(−7)	1.9(−7)	1.6(−7)	1.2(−6)	1.8(−6)	6.3(−6)
NIV	8.0(−4)	3.3(−4)	3.5(−4)	2.4(−4)	6.9(−4)	7.4(−4)	7.5(−4)
NV	3.4(−6)	5.0(−4)	4.8(−4)	4.3(−4)	1.3(−4)	8.4(−5)	6.9(−5)
OIV	6.6(−4)	5.9(−4)	6.1(−4)	6.0(−4)	6.5(−4)	6.5(−4)	6.5(−4)
OV	2.7(−7)	7.0(−5)	5.1(−5)	4.0(−5)	8.0(−6)	6.6(−6)	8.8(−6)
OVI	7.6(−15)	4.9(−10)	5.4(−9)	1.6(−5)	4.8(−7)	2.5(−7)	2.7(−7)
SiIV	5.5(−7)	2.2(−8)	1.1(−8)	5.3(−9)	1.4(−7)	2.2(−7)	2.7(−7)
SiV	4.2(−5)	4.2(−5)	4.2(−5)	8.9(−6)	2.0(−5)	2.6(−5)	2.8(−5)
PV	2.0(−7)	2.4(−8)	2.2(−8)	1.0(−7)	2.3(−7)	2.3(−7)	2.3(−7)
PVI	1.9(−8)	2.1(−7)	2.1(−7)	9.1(−8)	7.9(−9)	3.9(−9)	2.5(−9)
SIV	2.5(−6)	7.3(−9)	6.7(−9)	2.5(−8)	6.2(−8)	6.1(−8)	6.1(−8)
SV	1.4(−5)	4.7(−6)	4.7(−6)	7.5(−6)	1.6(−5)	1.7(−5)	1.7(−5)
SVI	3.2(−7)	1.2(−5)	1.2(−5)	6.0(−6)	3.6(−7)	1.9(−7)	1.5(−7)
FeV	3.8(−5)	1.6(−5)	1.6(−5)	3.9(−6)	2.8(−5)	3.3(−5)	3.4(−5)

We conclude that if the mass-loss rate is really as high as in model 2, we need a higher effective temperature to reduce the strengths of the Fe IV lines and of Si IV and C III.

3.2.2. Models at higher $T_{\rm eff}$: the best model

We have calculated a grid of self-consistent models for Melnick 42 with effective temperatures higher than 42 000 K up to 55 000 K. Since the radius is determined by the distance to the LMC and the dereddened V-magnitude (see Heap et al.), where the latter is in the Rayleigh–Jeans-domain of the spectrum, the relation

$$R_*(T_{\rm eff}) = R_*(42\,500\ {\rm K}) * (T_{\rm eff}/42\,500\ {\rm K})^{1/2}$$

was used. The gravity was adjusted so that the wind model reproduced the observed terminal velocity (see Sect. 3.1).

Table 6. The wind models of Melnick 42

model	$T_{\rm eff}$	log g	$R_*/R_\odot$	blocking	shocks	log $L_x/L_{\rm bol}$	v_t/v_∞	γ	m	$Z/Z_\odot$	$\dot{M}$ ($10^{-6} M_\odot$/yr)
1	42.5	3.5	28	hydrostatic (N)LTE	yes	- 7.3	0.045	1.	1.	0.25	4.0
2	42.5	3.5	28	hydrostatic (N)LTE	yes	- 7.3	0.045	1.	1.	0.25	27.0
3	50.5	3.785	26	hydrostatic (N)LTE	yes	- 6.4	0.045	1.4	3.2	0.25	27.0
4	50.5	3.785	26	hydrostatic (N)LTE	no	- 6.4	0.045	1.4	3.2	0.25	27.0

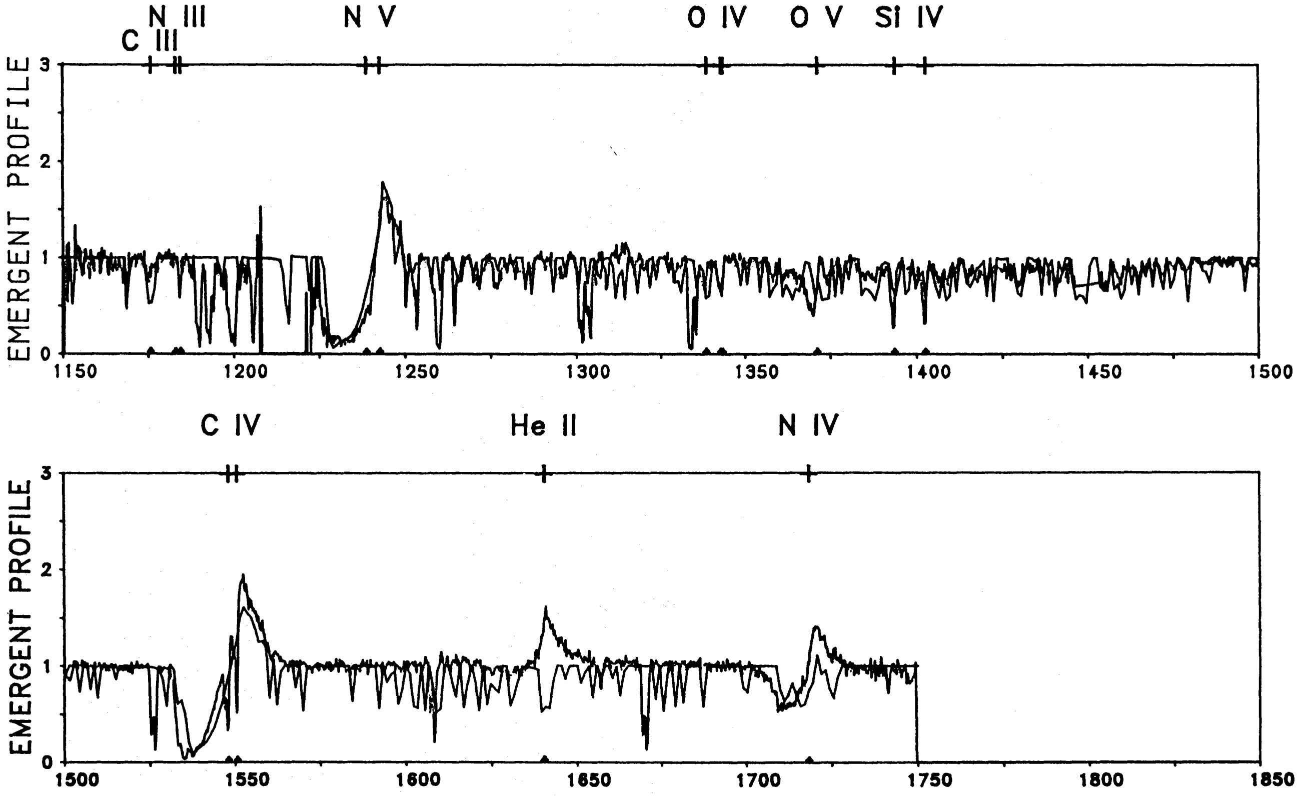

a

Fig. 13a and b. Calculated and observed UV spectra for Melnick 42. The calculated spectra are from model 1, where the low effective temperature deduced from a photospheric analysis has been assumed. The observed spectrum shows the HST high resolution observation obtained by Heap et al. (1991). The result of the self-consistent calculation is shown in **a**, whereas an artificially high mass loss rate has been assumed for the model calculation (model 2) shown in **b**

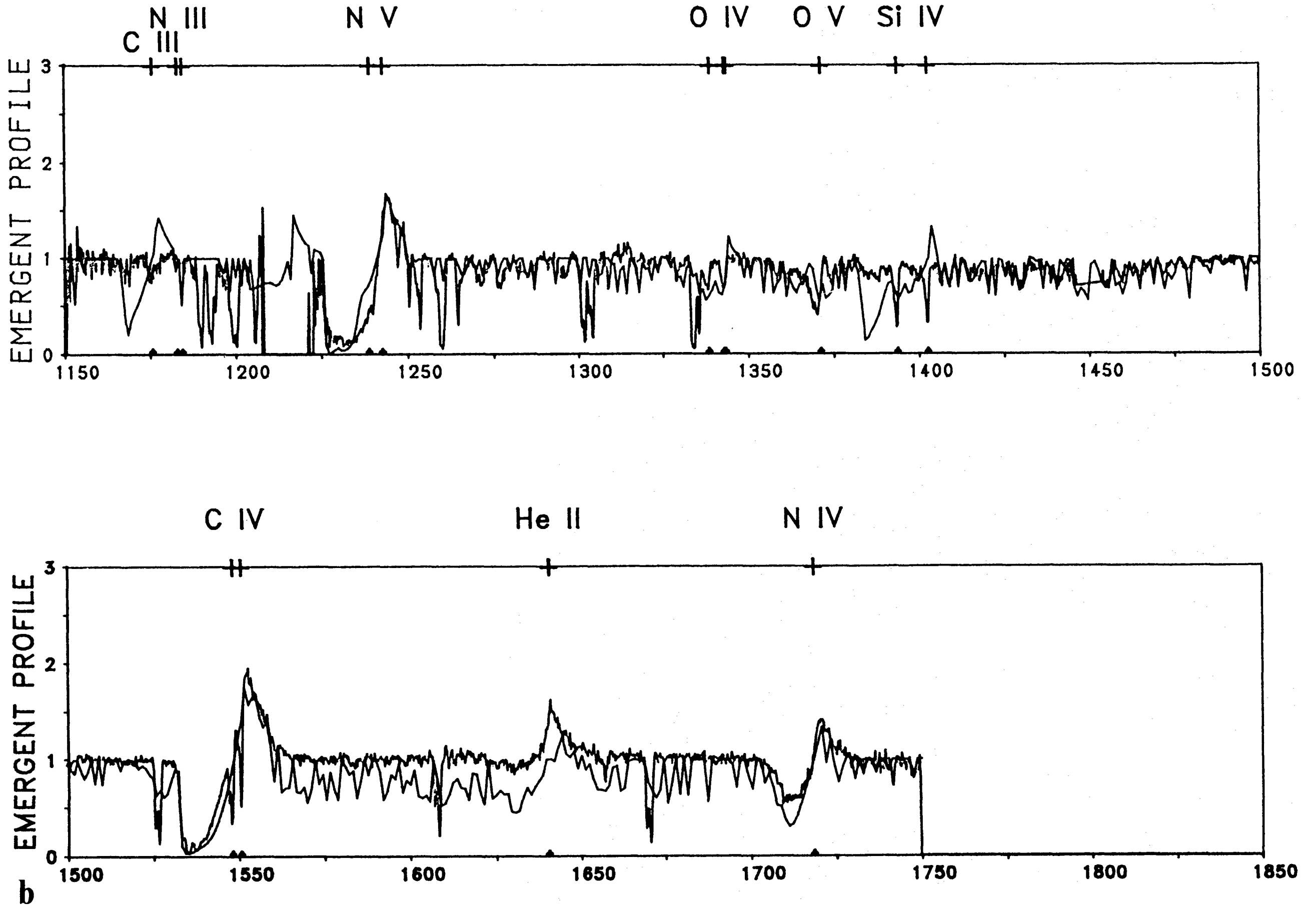

Fig. 13 (continued)

1/4 solar abundance was assumed for all elements heavier than helium.

The best fit of $T_{\rm eff}$, obtained from the Fe V/IV ionization equilibrium, the Si IV and the C III line gives

$$T_{\rm eff} = 50\,500\,{\rm K}\,, \quad \log g = 3.785\,, \quad R_*/R_\odot = 26\,,$$

$$M/M_\odot = 150.4\,, \quad \log(L/L_\odot) = 6.6\,.$$

The mass-loss rate and the terminal velocity of the corresponding self-consistent wind model are

$$\dot{M} = 27\;10^{-6} M_\odot\,{\rm yr}^{-1}\,, \quad v_\infty = 3025\,{\rm km\,s}^{-1}\,.$$

The depth independent force multiplier parameters that reproduce these values are

$$k = 0.065\,, \quad \alpha = 0.70\,, \quad \delta = 0.08\,.$$

The mass-loss rate is increased considerably as a result of the enhanced luminosity. The EUV line blocking, which modifies the radiation field below the hydrogen Lyman edge considerably in this model as well (model 3, see Table 6), was approximated by a procedure similar to that described in Sect. 3.1.2 (see Fig. 14c; the line blocked fluxes for Melnick 42 in this approximation are given by the following $T_{\rm rad}$: 45 000 K in the range 227–300 Å, 40 000 K in the range 300–460 Å, 36 000 K in the range 460–911 Å; note further that compared to ζ-Pup less blocking occurs shortward of 300 Å due to the higher temperature).

Figure 14a compares the synthetic spectrum of this model with the observations. The improvement for He II 1640 and N IV is striking. The Fe V lines are well reproduced and the Fe IV lines have disappeared as observed. Si IV is weak as observed due to the high $T_{\rm eff}$ despite the high $\dot{M}$ (note that the observations have an interstellar contribution). C III is at least in qualitative agreement and the same is true for O IV and O V.

The good fit of N V and, in particular of C IV including its unsaturated broad absorption trough is a result of the relatively soft shock emission (see Sect. 3.2.1) for which the X-ray luminosity was adjusted to $\log{(L_X/L_{\rm Bol})} = -6.4$. Figure 14b, which displays the synthetic spectrum of model 4 calculated for the same hydrodynamic structure but without shock emission, demonstates that the shock radiation field is needed to desaturate the C IV resonance line by ionization to C V. N V is slightly too weak without shocks and enhanced by additional ionization from N IV to N V and in the outer-most part reduced by ionization from N V to N VI if shocks are included. This is also seen from the N IV line which becomes weaker if shocks are included. We add here, that model three was calculated with $\gamma = 1.4$ and $m = 3$ (see Sect. 2.4). In this way the shock emission is shifted towards the outer high velocity wind layers ($R > 3R_*$) and the observed N IV profile remains in agreement with the observations.

3.2.3. Discussion of effective temperature, evolutionary status and abundances

From models 2 and 3 it is obvious that a high mass-loss rate, as indicated by the strengths of the optical Hα and He II 4686 emission lines, provides a solution to the previous problems encountered when synthesizing the whole UV spectrum including the He II 1640 line, if accompanied by a considerably increased effective temperature. This result found from the diagnostics of UV NLTE line formation is completely consistent with the hydrodynamics of radiation driven wind theory. The reason is obvious. For a given radius an increased T_{eff} results in an enhanced luminosity and with the gravity deduced from the observed terminal velocity MK 42 is now extremely close to the Eddington-limit (the ratio of stellar to Eddington-luminosity is 0.7). As a consequence, an extremely high mass-loss rate is obtained.

With the stellar parameters derived in Sect. 3.2.2 Mk 42 is the most massive and most luminous star known. It is, of course, extremely important to check whether these parameters are in accordance with stellar evolution theory.

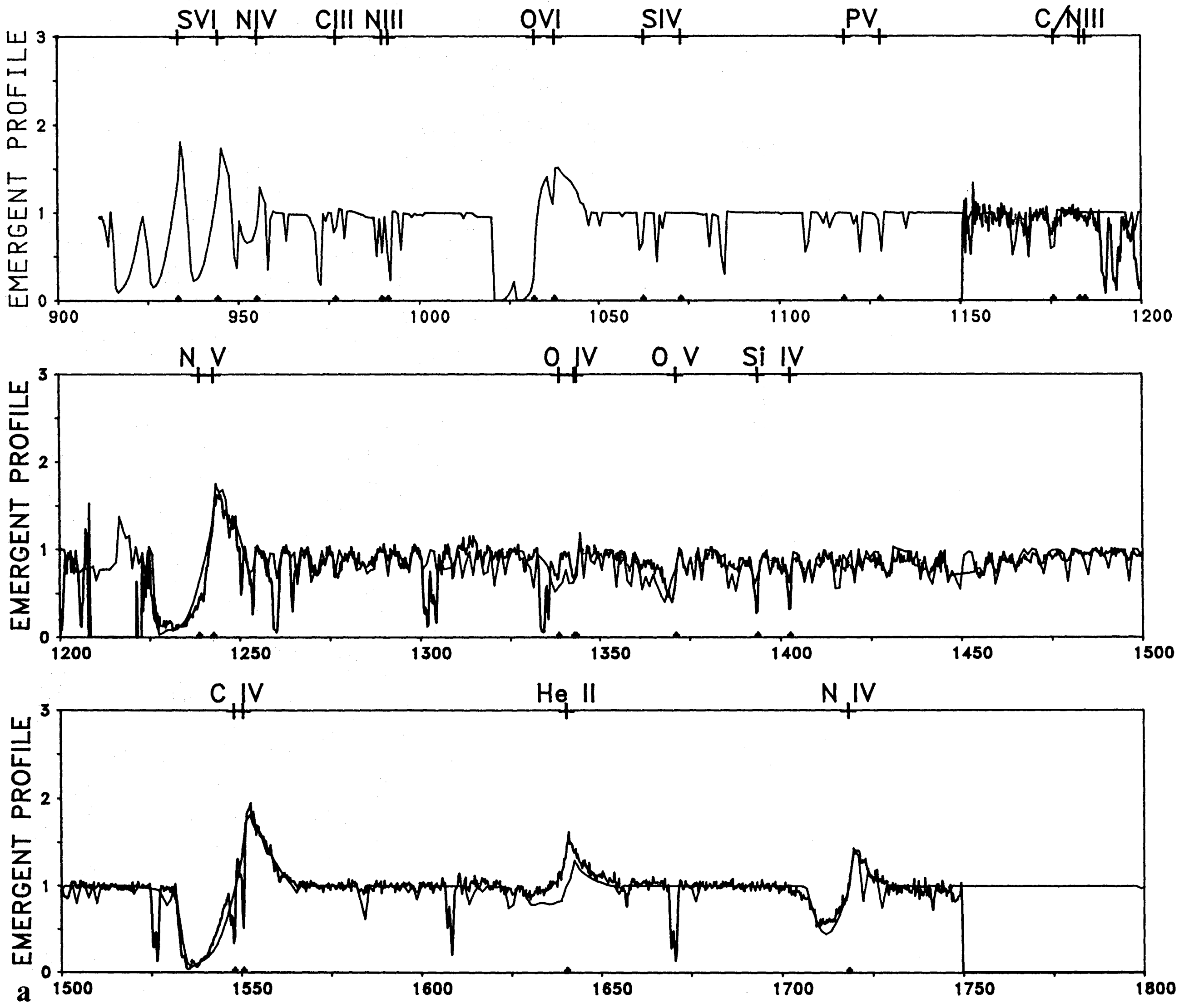

Fig. 14a–c. Same as Fig. 13, but for our current best model (3), where the stellar parameters have been determined using our procedure. In **a** the predicted spectrum in the frequency range of 912–1150 Å is also shown. For the computation shown in **b** the shock emission coefficient has been neglected (model 4). **c** Logarithm of the emergent flux (erg cm^{-2} s Hz^{-1}) of a photospheric model of Mk 42 in the range 227–911 Å. The smoothed mean structure assumed for our procedure is also shown (dashed)

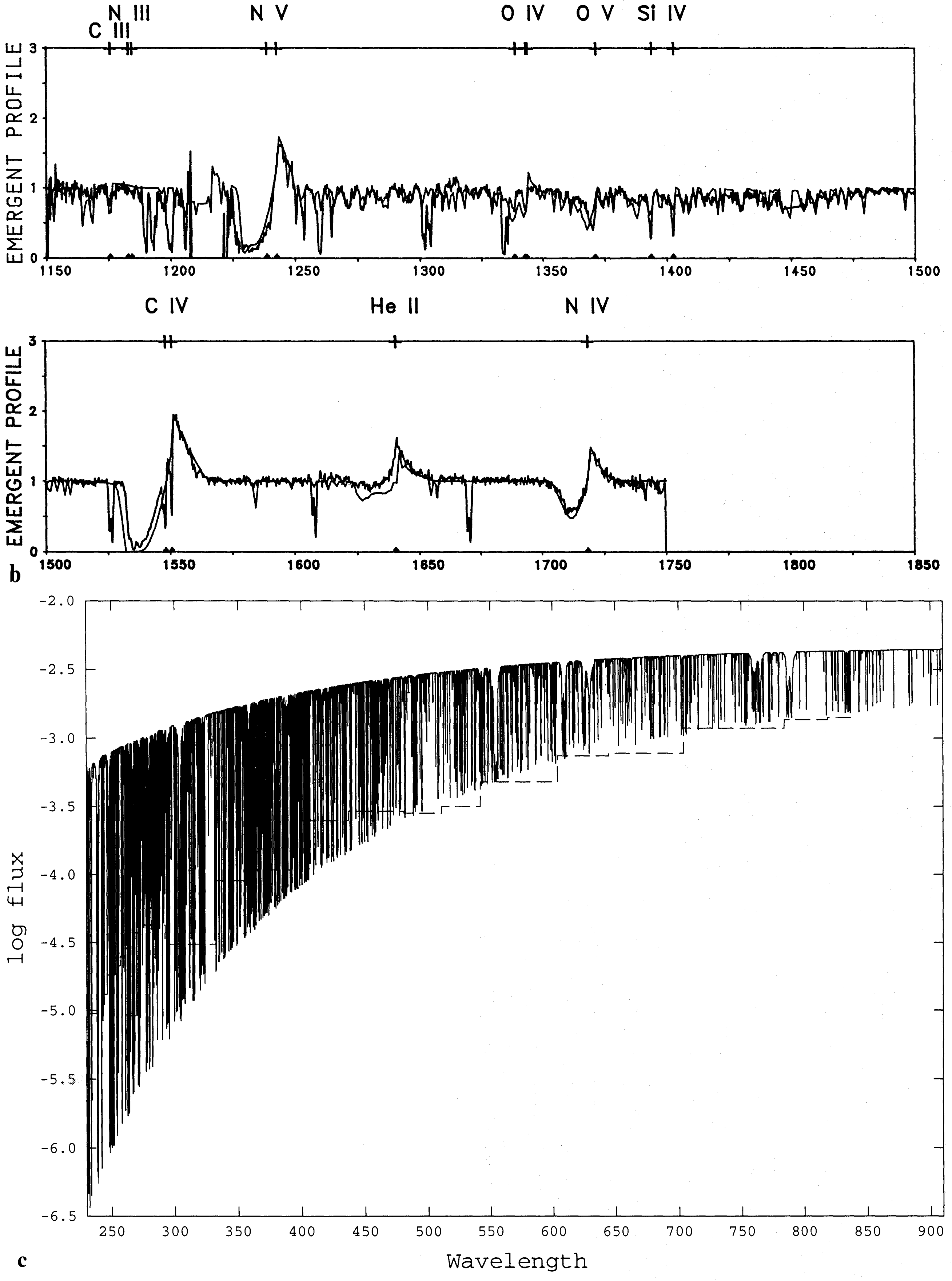

Fig. 14 (continued)

A first step is to examine whether mass and luminosity agree with the theory. For this purpose, we have extrapolated Maeder's (1990) evolutionary tracks (for 1/4 solar metallicity) at $\log T_{\rm eff} = 4.7$ to a luminosity of $\log (L/L_\odot) = 6.6$ and found a mass of $155 M_\odot$. This agrees well with the $150 M_\odot$ determined by our analysis. Mk 42, therefore, does not show indications of the "mass discrepancy" that was found for many galactic O-stars by Groenenwegen et al. (1989), Herrero et al. (1992) and in Paper X.

Interestingly, Mk 42 does not expose CNO-processed material at its surface. This agrees with the conclusion of Herrero et al. that the results of the CNO-process are seen in the atmospheres of O-stars, if a severe "mass discrepancy" is encountered.

Although the higher effective temperature solved the diagnostical problems and led to a better understanding of the object a severe problem remains. This concerns the lower effective temperature obtained by Heap et al. (1991) from an analysis of the optical hydrogen and helium absorption lines using hydrostatic NLTE atmospheres. In particular the presence of the He I λ4471 line in absorption with roughly 250 mÅ equivalent width was decisive for this analysis, since this feature cannot be fitted by means of a standard low gravity hydrostatic NLTE model atmosphere at an effective temperature considerably higher than 42 500 K (see Kudritzki 1980; Simon et al. 1983; Paper X). To disentangle this proplem we have to investigate whether the He I λ4471 line can be reproduced at least qualitatively by means of our calculated model 3, and secondly to explain why standard hydrostatic NLTE models fail for extreme cases such as Mk 42.

Regarding the first point we calculated the profile of He 4471 using the NLTE temperature structure displayed in Fig. 16c. We investigated two cases, the inclusion of line blocking in the approximation outlined in the section above and the neglect of line blocking, i.e. only hydrogen and helium opacity was taken into account, as was done for the hydrostatic models used by Heap et al. The result is very interesting. The line is completely absent in the non-blocking case, but has a reasonable strength (125 mÅ), when blocking is included. While this is certainly not a quantitative reproduction of the observations, it indicates qualitatively that a proper treatment of EUV line blocking is obviously important for helium line formation in the presence of dense stellar winds.

In order to understand how the EUV line blocking can affect the strength of a weak He I optical absorption line,

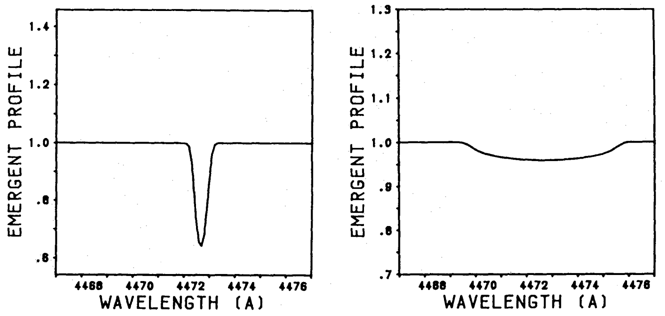

Fig. 15. Profiles of He I λ4471 resulting from our current best model (3) for Melnick 42 (left without rotational broadening, right with $v_{\rm rot} = 200\ {\rm km\ s^{-1}}$

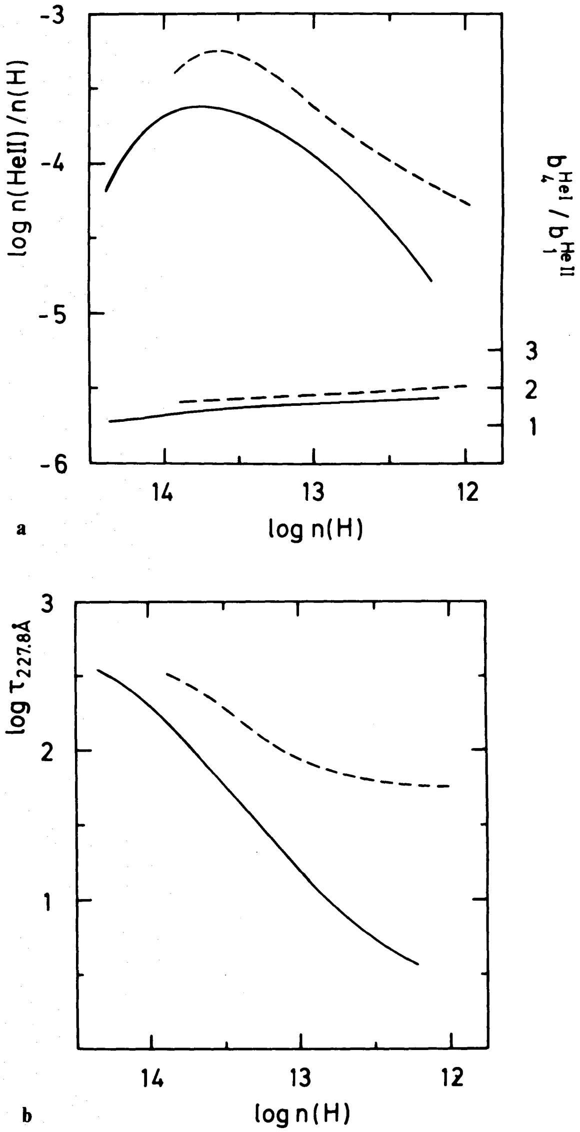

Fig. 16. **a** Logarithm of the number fraction of He II in units of the hydrogen particle number (upper curves); logarithmic departure coefficient for the 4th level of He I (i.e. the lower level of the He I λ4471 line) in units of the He II ground level departure coefficient (lower curves); logarithm of the optical depth at the He II ground state threshold **b** as a function of $\log n$ (H). Dashed: model including EUV line blocking, fully drawn: model neglecting line blocking. **c** Temperature versus density in the wind part of Melnick 42 (model 3). The fully drawn curve represents a spherical NLTE-model which includes H and He opacities, while the dashed curve corresponds to a spherical grey model

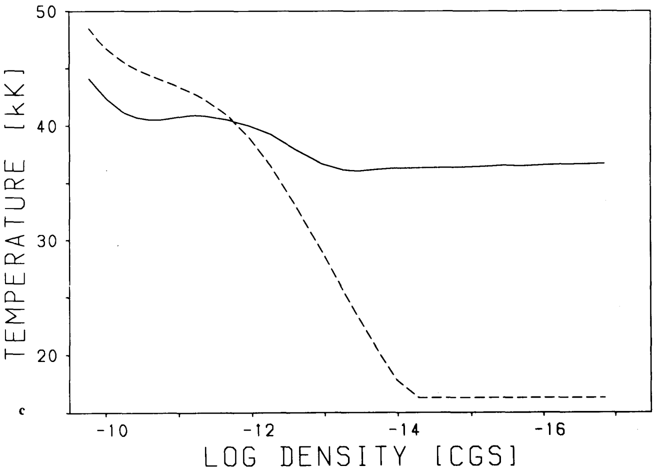

Fig. 16 (continued)

a detailed comparison of the He ionization fractions resulting from these models is required. Since the levels of the He I 4471 line belong to the triplet system the departure coefficient of the lower level is coupled to the departure coefficient of the He II ground level via ionization and recombination processes. This is verified in Fig. 16a for both models. The strength of the He I line thus depends directly on the ionization fraction of He II. In Fig. 16a it is additionally shown that model 3; which includes line blocking yields a considerably increased He II ionization fraction (see also Sect. 3.1.2). This is initially caused by the suppressed pumping of the He II resonance line into the first excited level and a reduced photoionization rate from this level. Both effects are caused by EUV line blocking. This behaviour influences the optical thickness shortward of the He II ground state edge. Note that the strength of this influence depends mostly on the mean wind density, for ex-

Table 7. Important ionization ratios ($n_{\rm I}/n_{\rm H}$) for model 3 of Melnick 42

R	1.002	1.040	1.64	2.25	4.0	8.6	76.0
v/v_∞	0.0008	0.06	0.47	0.64	0.81	0.91	0.99
$T_e/T_{\rm eff}$	0.97	0.82	0.58	0.48	0.36	0.34	0.33
T_s (10^6K)	-	-	-	-	0.15	0.21	0.28
n_H (cm^{-3})	9.1(11)	7.2(13)	4.6(10)	1.8(10)	4.5(9)	8.7(8)	1.0(7)
HeII	3.7(-4)	5.8(-5)	1.3(-4)	4.2(-4)	8.1(-6)	3.3(-6)	2.8(-6)
CIV	8.4(-6)	2.6(-6)	1.5(-5)	5.2(-5)	8.3(-8)	3.3(-8)	2.1(-8)
NIV	8.3(-6)	4.9(-6)	1.7(-5)	1.5(-5)	6.8(-10)	7.3(-11)	2.2(-11)
NV	1.6(-5)	1.9(-5)	6.7(-6)	7.8(-6)	5.3(-7)	1.6(-7)	8.2(-8)
OIV	1.6(-4)	1.3(-4)	1.9(-4)	2.0(-4)	3.6(-7)	6.5(-9)	6.6(-11)
OV	5.0(-5)	8.0(-5)	1.1(-5)	3.3(-6)	5.3(-6)	5.3(-7)	1.1(-7)
OVI	1.2(-8)	9.7(-9)	1.7(-8)	4.1(-7)	1.1(-4)	4.2(-5)	1.9(-5)
SiIV	2.3(-8)	1.5(-9)	5.6(-10)	3.6(-10)	3.4(-11)	4.7(-12)	6.9(-13)
SVI	3.1(-6)	3.5(-6)	3.2(-6)	2.2(-6)	5.2(-8)	1.8(-8)	1.0(-8)
FeV	3.2(-6)	1.3(-6)	2.5(-6)	1.4(-6)	4.0(-12)	1.3(-13)	1.8(-14)

tremely dense winds like Mk 42 a considerable effect results (see Fig. 16b). Due to the increased optical thickness the radiation field is significantly reduced since the coupling to the local temperature becomes stronger. This in turn increases the ionization fraction of He II further, even in the deeper layers where the He I line is formed.

We therefore conclude that the different density structure, compared to hydrostatic calculations, caused by the extremely high mass loss rate, means that the EUV blocking influences even deeper regions where weak absorption lines are formed (this idea might also be important for the analyses of Wolf–Rayet stars). We conclude further that as long as photospheric blocking is not taken into account properly in the analyses of optical spectra the derived stellar parameters might be uncertain for objects with extremely high mass loss rates. Moreover, we cannot rule out at the moment that objects with smaller mass loss rates are also affected.

3.2.4. Ionization fractions

In Table 7 we give information on the most important ionization ratios obtained for our model of Melnick 42. The ratios are presented at 7 characteristic radial points, for which the velocities, the local electron temperatures and the shock temperatures are also given. In view of the discussion in Sect. 3.2.2 the sudden increase and decrease of high and low ionization stages, respectively, at the radius where the influence of the shocks first becomes apparent is not surprising. We note again that this behaviour is responsible for the fact that the C IV and N V resonance lines are not completely saturated, and it also explains that the assumption of smaller values of $R_{\rm min}$ and γ decreases the ionization stages of N IV and He II drastically in regions where the corresponding spectral lines are still observed. Thus, the parameters of the shock radiation description are constrained by the profiles of these lines.

A comment is also necessary concerning the line force, since this is also influenced by the sudden shift in ionization stages. However, as observed in Table 7, the changes in ionization occur at velocities ($v > 0.8v_\infty$) where the terminal velocity is almost reached, and since the different high ionization stages have sufficient lines to be able to accelerate the wind, the influence is not dramatic. Should this occur at lower velocities, however, large effects would be apparent and as a result much lower terminal velocities would be obtained.

4. Summary and future work

The main objective of this work was to investigate whether information about stellar parameters, abundances and plasma conditions can be extracted from UV high resolution spectra by means of stellar wind NLTE spectral synthesis. For this purpose, we have applied improved theoretical models of radiatively driven stellar winds. The improvements removed some deficiencies in previous models, such as the inaccuracy of atomic data, the underestimation of photospheric EUV line blocking and the neglect of radiative losses by shock heated matter.

In overcoming these shortcomings we have updated the atomic data used for the most important ionization stages. The photospheric line blocking is now treated in a more realistic but admittedly still approximate way. In future, this will be further improved by means of a completely self-consistent treatment which is presently being developed. We have shown that the radiation emitted by shock heated matter at typical temperatures ($\sim 10^6$ K) in the EUV is the dominant source of ionization required to explain the problem of "superionization". We have incorporated this source in a preliminary way based on an approximate calculation of the shock emission coefficient. In a next step, we will replace this emission coefficient by a detailed treatment of the individual shock emission lines. We will further account for the mutual influence of shocks by absorption processes and the Auger-ionization, and consider the real structure of individual shocks by means of detailed time dependent hydrodynamics calculations (all this work is under way).

That this effort is worthwhile has been shown by the quantitative spectroscopic analyses accomplished for two O-stars. In the case of ζ-Pup we obtained a higher mass loss rate due to the use of improved atomic data. This is not only consistent with radio observations, but also reduces the discrepancies between a number of predicted and observed spectral lines. We also found that $\rm He^{++}$ recombines in the outer wind and that this influences the spectrum considerably. We further found that the wind temperature is below $= 0.6T_{\rm eff}$ in the outer portions of the wind. From this we concluded that the energy equation of a stationary wind describes the temperature of the cool unshocked wind material rather well, but that a less elaborate (grey) temperature structure is also useful for our purposes, since the UV spectra depend only weakly on details of the local temperature. From our description of the shock radiation, which solves the problem of "superionization", we deduced first rough information about the form and the spatial dependence of shock temperatures and jump velocities. We also came to the unexpected conclusion that the shock emission may also influence the infrared and radio regime of the spectrum. With regard to the abundances it transpired that in particular the relative abundances of carbon and nitrogen can be determined very precisely.

For Melnick 42 we derived much higher effective temperature, mass and luminosity together with a much higher mass loss rate than Heap et al. who used hydrostatic atmosphere models for the determination of stellar parameters. Additionally, abundances a factor four smaller than solar were obtained for this LMC object. No indication for CNO processed matter was found. Mass and luminosity agree with stellar evolution theory.

We concluded further that photospheric blocking influences the optical analyses considerably at least in cases where the objects are subject to extremely high mass loss. This conclusion leads to the cautious speculation that Wolf–Rayet stars, which do indeed have high mass loss rates, might be closer to the Eddington–limit than suggested, for instance, by Schmutz et al. (1989). Finally, our description of shock radiation revealed that Melnick 42 not only has smaller shock temperatures than ζ-Pup, but that the emitted radiation is also concentrated towards the outermost part of the wind.

Acknowledgements. We wish to thank our colleagues Dr. T. Gehren, Dr. J.H.M.M. Schmitt, Dr. S. Voels, Dr. D.G. Hummer, Dr. R. Gabler, S. Haser, P. Najarro, Dr. J.I. Castor (referee) for helpful discussions and G. Taresch and Dr. M. Lennon for help in replacing the atomic data. It is also a pleasure to thank Dr. D. Morton for providing us with the Copernicus high resolution spectrum of ζ-Puppis. This research was supported by the Deutsche Forschungsgemeinschaft in the "Gerhard Hess Programm" under grant PA 477/1-1 and Ku 474/13-2.

Appendix A

Here we briefly discuss the analytical approximation of the filling factor used as a starting value in the procedure described in Sect. 2.4.

In order to find the starting value for the filling factor Eqs. 2 and 3 (assuming a β-velocity field with $\beta = 1$ for the local velocity) are inserted in Eq. (1c). This gives

$$\bar{\varepsilon}^{\rm s}_\nu(r) = d\frac{w^{1/2}}{r^4(1-1/R)^2}\,{\rm e}^{-\omega\nu w}\,, \tag{A1}$$

where $R = r/R_*$ and d, ω, w are defined as follows:

$$\begin{aligned}
d &= f/(v_\infty^2(A)^{1/2})\left(6.15\,10^8\,\dot{M}^2\frac{1+2Y_{\rm He}}{1+4Y_{\rm He}}\right)\,,\\
A &= \frac{3}{16}\frac{\mu m_{\rm H}}{k}v_{\rm turb}^2\,,\\
\omega &= h/(kA)\,,\\
w &= 1/\left[\left(1-\frac{1}{R}\right)^{2\gamma}+B\right]\,,\\
B &= \frac{11}{5}\left(\frac{a_{\rm s}}{v_{\rm turb}}\right)^2\,.
\end{aligned} \tag{A2}$$

We now start from

$$L_\nu = 8\pi^2r^2\int_0^1 I_\nu(\mu)\mu\,{\rm d}\mu\,. \tag{A3}$$

Here μ is the direction cosine between the radiation and the flow.

If we neglect the optical thickness in the X-ray regime for the moment, Eq. (A3) yields, after some algebra,

$$L_\nu = 8\pi^2R_*^3\int_{R_{\rm min}}^{R(v_\infty)}\bar{\varepsilon}^{\rm s}_\nu\left[1+\left(1-\frac{1}{R^2}\right)^{1/2}\right]R^2\,{\rm d}R\,. \tag{A4}$$

Inserting Eq. (A4) into Eq. (4) we obtain after substituting dw for dR

$$\begin{aligned}
L_x = \frac{8\pi^2 d}{R_*\omega}\Bigg\{\omega\int_{\Delta\nu_x}\int_{w(R_{\rm min})}^{w(v_\infty)} &\times\left[\frac{1+(1-1/R^2)^{1/2}[(1-1/R)^{2\gamma}+B]^{3/2}}{2(1-1/R)^{2\gamma+1}}\right]\\
&\times {\rm e}^{-\omega\nu w}\,{\rm d}w\,{\rm d}\nu\Bigg\}\,.
\end{aligned} \tag{A5}$$

By replacing the term in the brackets { } by C the factor d is given by

$$d = \frac{L_x R_*\omega}{8\pi^2 C}\,. \tag{A6}$$

Since the term in square brackets in Eq. (A5) approaches unity for not too small radii, C can be evaluated analytically with sufficient accuracy (numerical checks have shown that the accuracy is to within a few percent even in the worst case). For the case of a thin wind we can also find an estimate of the luminosity resulting solely from the post shock emission at each frequency

$$L_\nu \simeq \frac{L_x}{C}\frac{{\rm e}^{-\omega\nu}-{\rm e}^{-\omega\nu w(R_{\rm min})}}{\nu}\,. \tag{A7}$$

However, it should be noted that the correct value of L_ν must be calculated by incorporating $\bar{\varepsilon}^{\rm s}_\nu$ into the exact continuum radiative transfer.

References

Abbott D.C., 1982, ApJ 259, 282

Abbott D.C., 1985, Radio Stars. Reidel, Dordrecht, p. 219

Abbott D.C., Bieging J.H., Churchwell E., 1980, ApJ 238, 196

Abbott D.C., Bieging J.H., Churchwell E., Torres A.U., 1986, ApJ 303, 239

Barlow M.J., 1990, in: Haynes R., Milne D. (eds.) The Magellanic Clouds, Proc IAU Symp. 148, p. 291

Bieging J.H., Abbott D.C., Churchwell E.B., 1989, ApJ 340, 518

Bohannan B., Abbott D.C., Voels S.A., Hummer D.G., 1986, ApJ 308, 728

Cassinelli J.P., Olson G.L., 1979, ApJ 229, 304

Cassinelli J.P., Swank J.H., 1983, ApJ 271, 681

Castor J., Abbott D.C., Klein R., 1975, ApJ 195, 157

Castor J.I., 1979, Proc. IAU Symp. 83, p. 175

Castor J.I., 1987, in: Lamers H.J.G.L.M., de Loore C.H.W. (eds.) Instabilities in Luminous Early Type Stars. p. 159

Chlebowski T., Harnden F.R. Jr., Sciortione S., 1989, ApJ 341, 427

Chen W., White R.L., 1991, ApJ 366, 512

Cox D.P., Raymond J.C., 1985, ApJ 298, 651

Deltabuit E., Cox O., 1972, ApJ 177, 855

Dopita M.A., 1990, in: Haynes R., Milne D. (eds.) The Magellanic Clouds, Proc. IAU Symp. 148, p. 299

Drew J.E., 1989, ApJS 71, 267

Dufour R.J., 1984, in: van den Berg S., de Boer K.S. (eds.) Proc. IAU Symp. 108, Structure and Evolution of the Magellanic Clouds, Reidel, Dordrecht, p. 353

Ebbets D.C., 1982, ApJS 48, 399

Eisner W., Jones M., Nussbaumer H., 1974, Comput. Phys. Commun. 8, 270

Friend D., Abbott D.C., 1986, ApJ 311, 701 (Paper I)

Gabler R., Gabler A., Kudritzki R.P., Puls J., Pauldrach A.W.A., 1989, A&A 226, 162

Gabler R., Gabler A., Kudritzki R.P., Puls J., Pauldrach A.W.A., 1990, in: Garmany C.D. (ed.) Properties of Hot Luminous Stars, Boulder–Munich workshop, San Francisco; Astronomical Society of the Pacific Conf. Series, Vol. 7, p. 64

Gabler R., Kudritzki R.P., Mèndez R.H., 1991, A&A 245, 587

Gabler R., Gabler A., Kudritzki R.P., Mendez R.H., 1992, A&A 265, 656

Gabler R., 1992, Thesis, Ludwig-Maximilians-Universitaet, Muenchen

Gallagher J.W., Pradhan A.K., 1985, JILA Report No. 30

Gould R.J., 1978, ApJ 219, 250

Groenewegen M.A.T., Lamers H.J.G.L.M., 1989, A&AS 79, 359

Groenewegen M.A.T., Lamers H.J.G.L.M., Pauldrach A.W.A., 1989, A&A 221, 78

Hamann W.R., 1980, A&A 84, 342

Heap S.R., Altner B., Ebbets D., Hubeny I., Hutching J.S., Kudritzki R.P., Voels S.A., Haser S., Pauldrach A.W.A., Puls J., Butler K., 1991, ApJ 377, L29

Henrichs H.F., 1984, in: Rolfe E., Battrick B. (eds.) Proc. 4th European IUE Conf., Rome, ESA SP-218, p. 43

Henrichs H.F., 1986, PASP 98, 48

Herrero A., Kudritzki R.P., Vilches J.M., Kunze D., Butler K., Haser S., 1992, A&A 261, 209

Hillier D.J., Kudritzki R.P., Pauldrach A.W.A., Puls J., Baade D., Schmitt J.M., 1993, A&A (in press)

Howarth I.D., Prinja R.K., 1989, ApJS 69, 527

Hummer D.G., Rybicki G.B., 1985, ApJ 293, 258

Krolik J.H., Raymond J.C., 1985, ApJ 298, 660

Kudritzki R.P., 1980, A&A 85, 174

Kudritzki R.P., Simon K.P., Hamann W.R., 1983, A&A 118, 245

Kudritzki R.P., Hummer D.G., Pauldrach A.W.A., Puls J., Najarro F., Imhoff J., 1992, A&A 257, 655 (Paper X)

Kudritzki R.P., 1992, A&A 266, 395

Kurucz R.L., 1979, ApJS 40, 1

Kurucz R.L., 1992, Rev. Mex. Astron. Astrofis. 23, 181

Lamers H.J.G.L.M., Morton D.C., 1976, ApJS 32, 715

Lamers H.J.G.L.M., Rogerson I.B., 1978, A&A 66, 417

Lamers H.J.G.L.M., Gathier R., Snow T.P., 1982, ApJ 258, 186

Lamers H.J.G.L.M., Waters L.B., Wesselius P.R., 1984, A&A 134, L17

Langer J., Watson M., 1984, ApJ 284, 751

Leitherer C., 1988, ApJ 326, 356

Lucy L.B., Solomon P., 1970, ApJ 159, 879

Lucy L.B., White R., 1980, ApJ 241, 300

Lucy L.B., 1982, ApJ 255, 286

MacFarlane J.J., Cassinelli J.P., 1989, ApJ 347, 1090

Maeder A., 1990, A&AS 84, 139

Mihalas D., Hummer D.G., 1973, ApJ 179, 872

Mihalas D., 1978, Stellar Atmosphere, (2nd ed.). Freeman, San Francisco

Morton D.C., Underhill A.B., 1977, ApJS 33, 83

Nussbaumer H., Storey P.J., 1978, A&A 64, 139

Olson G.L., Castor J.I., 1981, ApJ 244, 179

Owocki S.P., Castor J.I., Rybicki G.B., 1988, ApJ 335, 914

Pakull W., 1992, Stellar Evolution and Interstellar Matter, Astronomische Gesellschaft Abstract Series No. 7. p. 86

Pauldrach A.W.A., Puls J., Kudritzki R.P., 1986, A&A 164, 86 (Paper I)

Pauldrach A.W.A., 1987, A&A 183, 295 (Paper III)

Pauldrach A.W.A., Herrero A., 1988, A&A 199, 262

Pauldrach A.W.A., Kudritzki R.P., Puls J., Butler K., 1990, A&A 228, 125 (Paper VII)

Pauldrach A.W.A., Puls J., 1990, A&A 237, 409 (Paper VIII)

Pauldrach A.W.A., Puls J., Gabler R., Gabler A., 1990, in: Garmany C.D. (ed.) Boulder–Munich Workshop, San Francisco, Astronomical Society of the Pacific Conference Series, Vol. 7, p. 171 (Paper IX)

Prinja R.K., Howarth I.D., 1986, ApJS 61, 867

Puls J., 1987, A&A 184, 227 (Paper IV)

Puls J., Hummer D.G., 1988, A&A 191, 87

Puls J., Pauldrach A.W.A., 1990, in: Garmany C. (ed.) Boulder–Munich Workshop; Astronomical Society of the Pacific Conference Series 7, p. 203

Raymond J.C., Smith B.W., 1977, ApJS 35, 419

Raymond J.C., 1988, in: Pallavicini R. (ed.) Hot Thin Plasmas in Astrophysics. Kluwer, Dordrecht, p. 3

Schmutz W., Hamann W.R., Wessolowski U., 1989, A&A 210, 236

Schmutz W., Schaerer D., 1992, Lecture Notes in Physics 401, 409

Seaton M.J., 1958, MNRAS 118, 504

Sellmaier F., Puls J., Kudritzki R.P., Gabler R., Gabler A., Voels S., 1993, A&A (in press)

Simon K., Jonas G., Kudritzki R.P., Rahe J., 1983, A&A 125, 34

Snow T.P., Morton D.C., 1976, ApJS 32, 429

Springmann U., Pauldrach A.W.A., 1992, A&A 262, 515 (Paper XI)

Voels S.A., Bohannan B., Abbott D.C., Hummer D.G., 1989, ApJ 340, 1073

Walborn N.R., Nichols-Bohlin J., Panek R.J., 1985, IUE Atlas of O-Type Spectra from 1200 to 1900 Angst., NASA Reference Publication 1155

Walborn N.R., Ebbets D.C., Parker J.W., Nichols–Bohlin J., White R.I., 1993, ApJ (in press)

Waldron W.L., 1984, ApJ 282, 256

Wright A.E., Barlow M.J., 1975, MNRAS 170, 41